Structural and Biological Properties of Heteroligand Copper Complexes with Diethylnicotinamide and Various Fenamates: Preparation, Structure, Spectral Properties and Hirshfeld Surface Analysis

Milan Piroš [1], Martin Schoeller [1], Katarína Koňariková [2], Jindra Valentová [3], Ľubomír Švorc [4], Ján Moncoľ [1], Marian Valko [5] and Jozef Švorec [1,*]

[1] Department of Inorganic Chemistry, Faculty of Chemical and Food Technology, Slovak University of Technology, Radlinského 9, 81237 Bratislava, Slovakia

[2] Institute of Medicinal Chemistry, Biochemistry and Clinical Biochemistry, Faculty of Medicine, Comenius University, Sasinkova 2, 81372 Bratislava, Slovakia

[3] Department of Chemical Theory of Drugs, Faculty of Pharmacy, Comenius University in Bratislava, Kalinčiakova 8, 83232 Bratislava, Slovakia

[4] Institute of Analytical Chemistry, Faculty of Chemical and Food Technology, Slovak University of Technology, Radlinského 9, 81237 Bratislava, Slovakia

[5] Department of Physical Chemistry, Faculty of Chemical and Food Technology, Slovak University of Technology, Radlinského 9, 81237 Bratislava, Slovakia

* Correspondence: jozef.svorec@stuba.sk; Tel.: +421-2-59325-625

Abstract: Herein, we discuss the synthesis, structural and spectroscopic characterization, and biological activity of five heteroligand copper(II) complexes with diethylnicotinamide and various fenamates, as follows: flufenamate (fluf), niflumate (nifl), tolfenamate (tolf), clonixinate (clon), mefenamate (mef) and N, N-diethylnicotinamide (dena). The complexes of composition: $[Cu(fluf)_2(dena)_2(H_2O)_2]$ (**1**), $[Cu(nifl)_2(dena)_2]$ (**2**), $[Cu(tolf)_2(dena)_2(H_2O)_2]$ (**3**), $[Cu(clon)_2(dena)_2]$ (**4**) and $[Cu(mef)_2(dena)_2(H_2O)_2]$ (**5**), were synthesized, structurally (single-crystal X-ray diffraction) and spectroscopically characterized (IR, EA, UV-Vis and EPR). The studied complexes are monomeric, forming a distorted tetragonal bipyramidal stereochemistry around the central copper ion. The crystal structures of all five complexes were determined and refined with an aspheric model using the Hirshfeld atom refinement method. Hirshfeld surface analysis and fingerprint plots were used to investigate the intermolecular interactions in the crystalline state. The redox properties of the complexes were studied and evaluated via cyclic voltammetry. The complexes exhibited good superoxide scavenging activity as determined by an NBT assay along with a copper-based redox-cycling mechanism, resulting in the formation of ROS, which, in turn, predisposed the studied complexes for their anticancer activity. The ability of complexes **1–4** to interact with calf thymus DNA was investigated using absorption titrations, viscosity measurements and an ethidium-bromide-displacement-fluorescence-based method, suggesting mainly the intercalative binding of the complexes to DNA. The affinity of complexes **1–4** for bovine serum albumin was determined via fluorescence emission spectroscopy and was quantitatively characterized with the corresponding binding constants. The cytotoxic properties of complexes **1–4** were studied using the cancer cell lines A549, MCF-7 and U-118MG, as well as healthy MRC-5 cells. Complex **4** exhibited moderate anticancer activity on the MCF-7 cancer cells with IC_{50} = 57 μM.

Keywords: copper(II) complexes; fenamates; Hirshfeld atom refinement; interactions with DNA; SOD mimetic activity

1. Introduction

Non-steroidal anti-inflammatory drugs (NSAIDs) are a very broad class of drugs that are widely used to treat conditions associated with acute or chronic inflammation,

such as pain or rheumatoid arthritis, and are also often used extensively for fever due to their analgesic or antipyretic effects [1–3]. A mode of their pharmacologic action is mostly based on the suppression of prostanoid production (important inflammatory mediators) by the inhibition of cyclooxygenase enzymes that catalyze prostanoid biosynthesis from arachidonic acid [3,4]. In addition, an alternative mechanism independent of cyclooxygenase inhibition was proposed [4]. This mechanism involves a direct effect of NSAIDs on mitochondria, leading to cellular oxidative stress and apoptosis [4]. From a chemical point of view, NSAIDs are predominantly weak acids that contain an acidic moiety together with an aromatic functional group. According to their chemical characteristics, NSAIDs can be roughly classified as derivates of carboxylic acids (salicylic, acetic and anthranilic), oxicams, sulfonamides or furanones [5].

Fenamates form a subgroup within NSAIDs and are derived from 2-anilinobenzoic (fenamic) acid. They are known to have anti-inflammatory, analgesic and antipyretic activities in animals or humans mainly through the inhibition of cyclooxygenases [6]. Typical examples of fenamates are mefenamic acid, used to treat mild or moderate pain; flufenamic acid, used to treat rheumatic disorders; and tolfenamic acid, known as the drug Clotam, used to treat migraine headaches or as a veterinary drug [7,8] (Scheme 1). The derivates of 2-phenylaminonicotinic acid, such as niflumic acid or clonixin (Scheme 1), are also formally included as fenamates. Like other fenamates, they are mostly used as analgesic and anti-inflammatory agents in the treatment of rheumatoid arthritis or for pain relief [7].
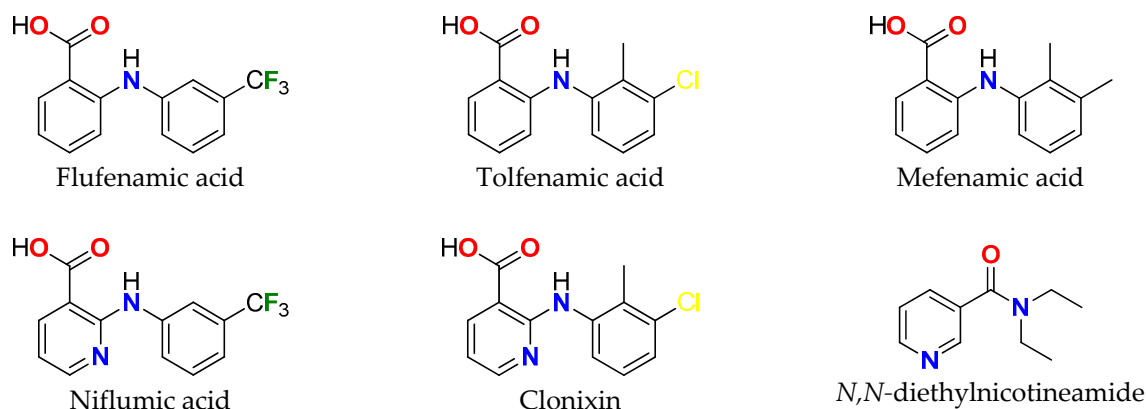
Scheme 1. Chemical formulae of used ligands.

Nicotinic acid derivatives, such as *N, N*-diethylnicotinamide, as well as nicotinamide or isonicotinamide, form an important class of heterocyclic pyridinecarboxamide compounds that are often used as a neutral N-donor ligand for the construction of hydrogen-bonded coordination networks and polymers [9]. Nicotinamide derivates alone exhibit interesting biological activities, including anticancer or anti-angiogenic properties, [10] and can exhibit herbicidal and antifungal activities [11].

Copper(II) complexes with NSAID ligands are now attractive objects for inorganic, pharmaceutical and medicinal chemists due to their potential to be effective anticancer, anti-inflammatory, antibacterial, antifungal or antiviral agents [12–17]. Such metal complexes often display lower toxicity and, at the same time, higher pharmaceutical efficiency than the parent NSAID drug. Ternary copper NSAID complexes containing other biologically active ancillary ligands (e.g. substituted pyridines or 1.10-phenantroline) offer a possibility how to successfully modify a coordination sphere of studied complexes toward desired activities [12,18–20]. Numerous copper complexes with NSAID, and especially with fenamates and *N*-donor ligands, such as pyridine and its derivates (2,2'-bipyridine and 1,10-phenanthroline), were studied by Psomas and coworkers [21–26]. These complexes show significant antioxidant activity, as well as an excellent ability to scavenge hydroxyl

and superoxide radicals [5]. Furthermore, copper complexes with meclofenamate show potential to be a successful anti-dementia agents [25].

In order to combine the proinflammatory ROS-mediating properties of copper(II) fenamate ligands and the ability to intercalate with the DNA of phenanthroline ligands, Simunkova and coworkers [27] prepared and studied three copper fenamates (tolfenamate, mefenamate and flufenamate) with 1,10-phenanthroline as potential anticancer copper compounds, giving the best results for a complex of the composition [Cu(fluf)$_2$phen]. Furthermore, Jozefíková and coworkers synthesized and investigated copper complexes with nicotinamide [28], isonicotinamide [29] and fenamates, showing that this type of complex exhibits promising biological activity, especially in the case of niflumate and clonixinate complexes.

In this context, we decided to prepare and characterize copper(II) complexes with dena ligands and various fenamates with the general formula of either [CuL$_2$(dena)$_2$] or [CuL'$_2$(dena)$_2$(H$_2$O)$_2$], where L = flufenamate (**1**), tolfenamate (**3**), mefenamate (**5**) and L'= niflumate (**2**) or clonixinate (**4**) in connection with their biological activity. Although the [CuL$_2$(dena)$_2$(H$_2$O)$_2$] (L = fluf [30], tolf [31] and mef [32]) and [Cu(nifl)$_2$(dena)$_2$] [33] complexes were already previously prepared and crystallograhically characterized, the solution of their crystal structure showed some flaws. As an example, the crystal structures of [Cu(tolf)$_2$(dena)$_2$(H$_2$O)$_2$] and [Cu(mef)$_2$(dena)$_2$(H$_2$O)$_2$] were solved without the inclusion of apparently resolved disorders, and in the latter case, the coordinates of the crystal structures were missing in the CCD database [31,32]. Moreover, the crystal structure of [Cu(nifl)$_2$(dena)$_2$] contains some incorrectly assigned atoms [33]. Taking these facts into account, we prepared all four complexes again. In addition, novel copper(II) complex with clonixinate anion and dena ligand with a composition of [Cu(clon)$_2$(dena)$_2$] was synthesized. Subsequently, single-crystal data of all five complexes were obtained at a low temperature (100 K) and high redundancy. In turn, the crystal structures of **1**–**5** were refined by means of an aspheric model using the Hirshfeld atom refinement (HAR) method, thus providing more precise structural parameters. The study of intermolecular interactions in the crystal structures of all complexes was augmented by the Hirshfeld surface analyses. Moreover, the structural and spectroscopic data of the complexes are discussed in connection with biological activity to find structure–activity relationship correlations. Our choice of fenamate ligands in this study was influenced by the observation that a pyridin ring containing analogs of copper fenamates shows better biological activity than their benzene analogs (niflumic vs. flufenamic and clonixin vs. tolfenamic acid) [29]. The presence of coplanarity of the aromatic rings in copper niflumates and clonixinate, in comparison with their copper flufenamate and tolfenamate analogs, may have had a substantial positive effect on the biological activity of the complexes, e.g., they could improve the intercalation ability of the complexes into DNA. In particular, the same substituents on the benzene ring in flufenamate and niflumate (trifluoromethyl susbtituent) or tolfenamate and clonixinate (chloro and methyl susbtituent) ligands provide the additional possibility for correlating the observed biological activities of the prepared complexes (Scheme 1).

In this regard complexes **1**–**5** were studied via various spectroscopic methods both in a solid state and in a DMSO solution, including IR, UV-Vis and EPR spectroscopy, as well as X-ray analysis. The redox properties of the complexes were studied via cyclic voltammetry. The SOD mimetic activity of all five complexes was determined with an indirect NBT assay. In order to compare the structure and biological activity of the complexes containing 2-anilinobenzoate and 2-phenylaminonicotinate ligands, the interaction of complexes **1**–**4** with calf thymus DNA (ct-DNA) was studied using absorption titrations, viscosity measurements and the ethidium bromide displacement fluorescence method. The interaction of these complexes with bovine serum albumin was investigated as well. Finally, the anticancer activity of complexes **1**–**4** was tested against several different cancer cell lines.

2. Results and Discussion

2.1. Synthesis

The complexes under study were obtained in moderate yields (57–75%) using a complexation reaction between corresponding fenamic acid and NaOH with copper acetate dihydrate and *N*, *N*-diethylnicotinamide (in a molar ratio of 2:2:1:2) in ethanol/methanol, according to Scheme 2. All five complexes are stable in the air, and their compositions were characterized with elemental analysis and IR spectroscopy, as well as with X-ray diffraction. The elemental analysis of the complexes is in agreement with the calculated values for the corresponding formulae: $[Cu(fluf)_2(dena)_2(H_2O)_2]$ (**1**), $[Cu(nifl)_2(dena)_2]$ (**2**), $[Cu(tolf)_2(dena)_2(H_2O)_2]$ (**3**), $[Cu(clon)_2(dena)_2]$ (**4**) and $[Cu(mef)_2(dena)_2(H_2O)_2]$ (**5**). The exact crystal structures and compositions of the complexes were fully confirmed via single-crystal X-ray crystallography.
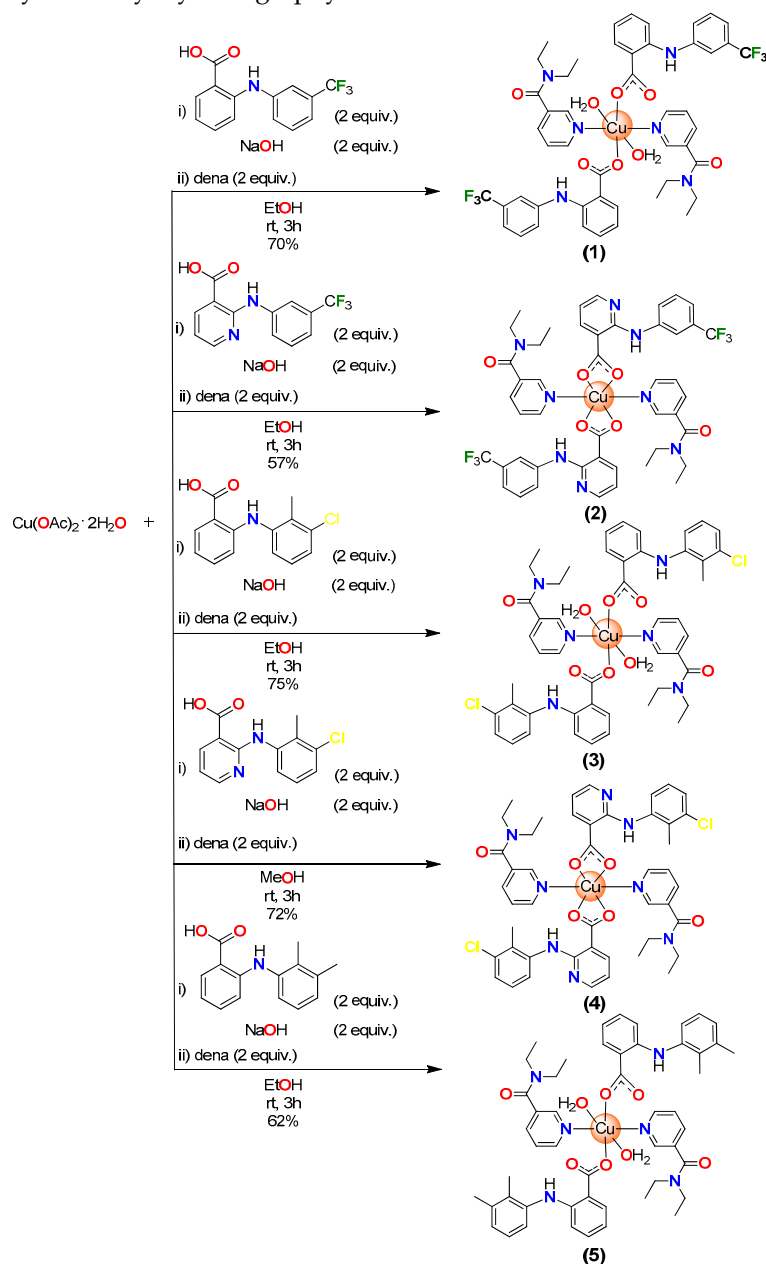
Scheme 2. Schematic representation of the syntheses of **1–5**.

2.2. IR and UV-Vis Spectroscopy

The infrared spectra of complexes **1–5** were recorded in the region of 4000–400 cm^{-1} in a solid state with the ATR technique, and a tentative description of some important bands was performed (Table 1) on the basis of literature data [34]. The spectra of all five complexes are shown in Supplementary Figure S1. According to the composition and spectral features, we can divide the studied complexes into two distinctive groups (**1, 3, 5** and **2, 4**). The IR spectra of **1, 3** and **5** showed broad absorption bands of medium intensity (3507, 3458 and 3473 cm^{-1} and 3324, 3217 and 3206, respectively) corresponding to the OH stretching vibrations (antisymmetric and symmetric, respectively) of coordinated water molecules, which were missing in the IR spectra of **2** and **4** (Supplementary Figure S1b), in accordance with the complex compositions. In addition, the IR spectra of all complexes in the region of 3200–3100 cm^{-1} exhibited a series of weak absorptions assigned to N-H vibrations, as well as a series of weak absorption peaks corresponding to CH stretches (between 3100 and 2800 cm^{-1}). Each IR spectra also contained a strong amidic band $\tilde{v}$(C=O) at 1629 cm^{-1} for **2** and **4** and at 1619, 1613 and 1612 cm^{-1} for **1, 3** and **5**. In the latter case, this band can be considered as a combined mixed band, caused by the vibration of the amidic C=O group and asymmetric $\tilde{v}_{as}$(COO^{-}) based on its strong intensity. In parent dena ligands, the band attributed to amidic C=O stretches could be found at 1630 cm^{-1}; thus, the coordination of the ligands resulted in the lowering of the band wavenumber only in the cases of complexes **1, 3** and **5**. C=N ring stretching vibrations in dena ligands appeared at 1592 cm^{-1}. After complex formations, this vibration moved to a lower wavenumber, with double sharp bands at 1581–1557 cm^{-1} in the cases of **1, 3** and **5** and at 1602–1582 cm^{-1} for **2** and **4**. Symmetric and antisymmetric carboxylate stretching vibrations could serve as an indication of a type of coordination mode for the carboxylate group in the prepared complexes. According to the literature [34], if the values of parameter Δ ($\tilde{v}_{as}$(COO^{-})-$\tilde{v}_{s}$(COO^{-})) are higher than those in ionic complexes, such as in sodium mefenamate (Δ = 190 cm^{-1}), the coordination mode of the carboxylate group is monodentate. In the cases of complexes **1, 3** and **5**, parameter Δ ($\tilde{v}_{as}$(COO^{-})-$\tilde{v}_{s}$(COO^{-})) fell in the range of 241–228 cm^{-1}, which is in a full accordance with the monodentate coordination mode of the carboxylate group. In the case of complexes **2** and **4,** parameter Δ showed values between 244 and 195 cm^{-1}, in agreement with the observed asymmetric bidentate chelating binding mode of the carboxylate group. Both bands belonging to the asymmetric and symmetric stretching vibrations of the carboxylate group were split, which could be attributed to the observed different *r*(Cu-O) bond length in the asymmetric bidentate chelating binding mode of the carboxylate group (Table 1). Moreover, bands belonging to the asymmetric stretching vibration were again found in the spectrum in the form of combined mixed bands caused by the coupled vibration of C=N and the carboxylate group based on their strong intensity.

Table 1. Infrared (in cm^{-1}) and electronic (in nm) data of complexes **1–5**.

Complex	$\tilde{v}$(O−H)	$\tilde{v}_{as}$(COO^{-})	$\tilde{v}_{s}$(COO^{-})	Δ	$\tilde{v}$(C=O)	$\tilde{v}$(C=N)	λ(d-d) [a]	λ(d-d) [b]
1	3057m 3324w	1619s [c] 1606s [c]	1378vs	241 228	1619s [c]	1581s 1568s	646br	795br
2	-	1595s [c] 1582s [c]	1387s 1368s	227/208 214/195	1629s	1595s [c] 1582s [c]	539br 615sh	791br
3	3458m,br 3206m,br	1613vs [c]	1377vs	236	1613s [c]	1579s 1557s	628br	789br
4	-	1602s [c] 1585vs [c]	1380s 1358vs	244/222 227/205	1629s	1602s [c] 1585s [c]	529br 612sh	794br
5	3473m,br 3217m,br	1612vs [c]	1376vs	236	1612s [c]	1575s 1561s	600br	801br

[a] nujol; [b] DMSO solution; [c] mixed bands; vs, very strong; s, strong; m, medium; w, weak; br, broad.

The electronic spectra of **1–5** were obtained in the solid state as nujol mulls, as well as in DMSO solutions. Representative examples of such spectra for complexes **4** and **5** are shown in Supplementary Figure S2. The solid-state spectra of the studied complexes showed very broad formally forbidden low-intensity d-d transitions in the visible region, with the maximum in the range of 587–648 nm, corresponding to the tetragonal bipyramidal stereochemistry around the metal center. In **2** and **4**, a shoulder at approximately 612–615 nm was observed (Table 1). In addition, the spectra also contained bands at approximately 200–400 nm, which could be considered as an intraligand transition, as well as a ligand-to-metal-charge transfer between the π electron cloud of the fenamate moiety and a central copper atom [18]. Upon dissolution in the DMSO solvent, the absorption maximum of broad *d-d* transitions shifted to higher wavelengths at a relatively constant range of 789–801 nm, which is expected for mononuclear copper complexes with distorted square planar geometry (Supplementary Figure S2 and Table 1) [35]. This shift likely indicates the potential coordination of DMSO solvent molecules in the primary coordination sphere of the complexes.

2.3. Molecular and Crystal Structures

The crystal structures of all five complexes were refined with a more accurate aspherical HAR method using data measured with high redundancy at 100 K. The crystal structures of four of the complexes, **1–3** and **5**, have been previously determined at room temperature using the standard IAM model, but the published crystal structures do not contain disordered groups and/or atomic coordinates in the CSD database [30–33]. On the other hand, complex **4** is newly synthesized, so its crystal structure is completely new. Complex **1** and the isostructural complexes **3** and **5** crystallize in a monoclinic system with the $P2_1/c$ (**1**) or $P2_1/n$ (**3**,**5**) space group, whereas complex **2** and the newly prepared complex **4** crystallize in the triclinic system with a *P*-1 space group. The molecular structures of all five complexes are shown in Figure 1, whereby the copper atoms in each case lie in a special position at the center of the symmetry. The selected bond distances of all complexes are listed in Table 2. The coordination polyhedron around the copper atom in complex **1**, as well as in isostructural complexes **3** and **5**, is in the shape of a tetragonal bipyramid. The equatorial plane is formed by a pair of oxygen atoms of monodentately bound carboxyl groups of flufenamate (**1**), tolfenamate (**3**) or mefenamate (**5**) anions (Cu1–O1 distances are in the range of 1.946–1.973 Å), and by two pyridine nitrogen atoms of *N*,*N*-diethylnicotinamide ligands (Cu1–N1 distances are in the range of 2.015–2.036 Å) in the *trans* positions. The two axial positions of the tetragonal bipyramid are complemented by two coordinated water molecules (Cu1–O1W distances are in the range of 2.435–2.488 Å). The molecular structures of complexes **1**, **3** and **5** are stabilized by intramolecular O–H⋯O hydrogen bonds between coordinated water molecules (O1W) and uncoordinated oxygen atoms of carboxyl groups (O2) (O1W–H1WA⋯O2; distances O1W⋯O2 are in the range of 2.728–2.738 Å; Supplementary Table S1). Fenamate (flufenamate, tolfenamate or mefenamate) anions also form intramolecular N–H⋯O bonds between amine nitrogen atoms (N3) and uncoordinated oxygen atoms of carboxyl groups (O2) (N3–H3⋯O2; distances N3⋯O2 are in the range of 2.631–2.658 Å). The complex molecules of **1**, **3** and **5** are connected into 1D supramolecular chains by means of intermolecular O–H⋯O hydrogen bonds between coordinated water molecules (O1W) and amide oxygen atoms of *N*,*N*-diethylnicotinamide ligands of neighboring complex molecules (O1W–H1WB⋯O3; distances O1W⋯O3 are in the range of 2.799–2.853 Å; Supplementary Table S1 and Supplementary Figure S8).

The crystal structures of complexes **2** and **4** are very similar and can be considered isostructural based on their similar cell parameters, same space group and similar molecular and intermolecular interactions. The coordination polyhedron around the copper atom in complexes **2** and **4** has the shape of a tetragonal bipyramid and is formed by two pairs of asymmetrically bonded oxygen atoms (O1,O2) of carboxyl groups of niflumate (**2**) or clonixinate (**4**) anions and by a pair of pyridine nitrogen atoms (N1) of *N*,*N*-diethylnicotinamide

ligands in the *trans* configuration. In both cases, the equatorial plane is equally formed by a pair of oxygen atoms (O1) (Cu1–O1; distances are 1.9502(6) and 1.9296(9) Å, respectively) and a pair of nitrogen atoms (N1) (Cu1–N1; distances are 2.0086(7) and 2.0170(12) Å, respectively). However, a significant difference can be observed in the distances between the two axially bonded oxygen atoms (O2). The Cu1–O2 distances are equal to 2.6467(11) Å in the case of complex **2**, but in the case of complex **4**, they are significantly extended to a value of 2.9554(10) Å. A similar trend was reported for several copper(II) carboxylate complexes with this type of coordination, where Cu–O_{ax} varied in the range of 2.45–2.98 Å [36].
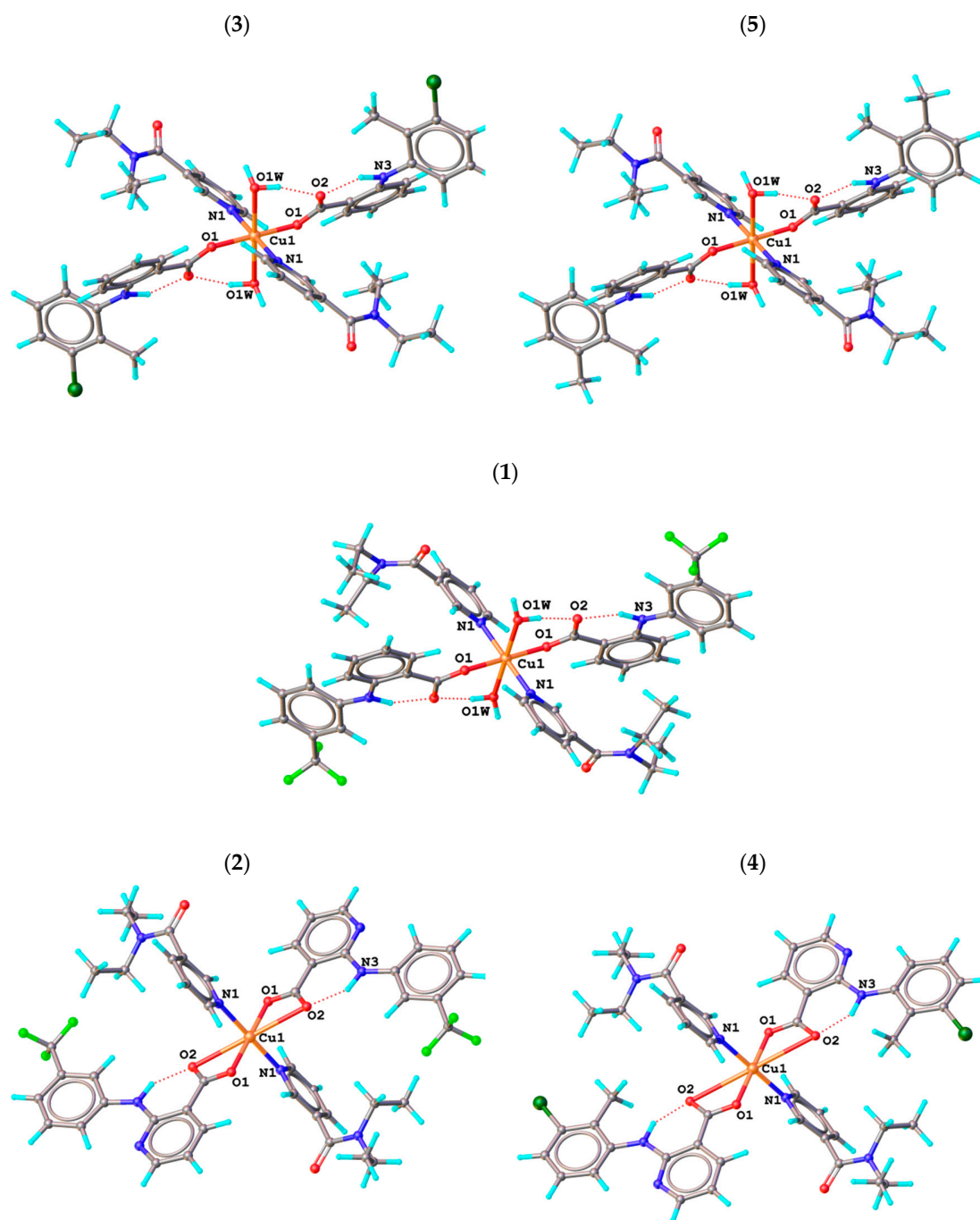
Figure 1. Molecular structures of [Cu(fluf)$_2$(dena)$_2$(H$_2$O)$_2$] (**1**), [Cu(nifl)$_2$(dena)$_2$] (**2**), [Cu(tolf)$_2$(dena)$_2$(H$_2$O)$_2$] (**3**), [Cu(clon)$_2$(dena)$_2$] (**4**) and [Cu(mef)$_2$(dena)$_2$(H$_2$O)$_2$] (**5**).

Table 2. Selected bond lengths (Å) for compounds (**1–5**).

	1 [i]	**3** [ii]	**5** [ii]
Cu1–O1	1.9726(9)	1.9465(5)	1.9475(7)
Cu1–N1	2.0149(11)	2.0345(6)	2.0364(9)
Cu1–O1W	2.4356(11)	2.4827(5)	2.4879(4)

	2 [iii]	**4** [iv]
Cu1–O1	1.9502(6)	1.9296(9)
Cu1–N1	2.0086(7)	2.0170(12)
Cu1–O2	2.6467(11)	2.9554(10)

Symmetry codes for a symmetrical part of a complex molecule: [(i)] 1–*x*, 1–*y*, 2–*z*; [(ii)] 1–*x*, 1–*y*, 1–*z*; [(iii)] 2–*x*, 1–*y*, 1–*z*; [(iv)] –*x*, 1–*y*, 1–*z*.

The aromatic pyridine (C12–C13–N4–C15–C16–C17) and benzene (C18–C19–C20–C21–C22–C23) rings of the niflumate (**2**) or clonixinate (**4**) anions are coplanar, which is also supported by intramolecular C–H⋯N hydrogen bonds between the carbon atoms of the benzene ring (C23) and the nitrogen atoms of the pyridine ring (N4) (C23–H23⋯N4; distances of C23⋯N4 are 2.913(1) and 2.899(2) Å, respectively; Supplementary Table S1). In addition, stabilization of the molecular structure can also be observed due to the intramolecular N–H⋯O bonds between amine nitrogen atoms (N3) and carboxylate oxygen atoms (O2) (N3–H3⋯O2; distances of N3⋯O2 are 2.669(1) and 2.673(2) Å, respectively). Coplanar pyridine and benzene rings of niflumate (**2**) or clonixinate (**4**) ligands are stacked with the neighboring complex molecules, resulting in the formation of π–π stacking interactions (Supplementary Figure S9) [37]. The angle between the plane of the pyridine ring and the plane of the benzene ring is 8.60° and 2.42°, respectively. The centroid–centroid distances are 3.72 and 3.60 Å, respectively, and the shift distances are 1.12 and 1.28 Å, respectively. Additionally, stacked complex molecules are also linked by means of C–H⋯O hydrogen bonds between the aromatic carbon atom (C21) and the carboxamide oxygen atom (O3) of *N*, *N*-diethylnicotinamide ligands of neighboring complex molecules (C21–H21⋯O3; distances of C21⋯O3 for both cases are identically equal to 3.4356(18) Å) in the 1D supramolecular chains. In the crystal structures of both complexes, other C–H⋯O hydrogen bonds can also be observed between the carbon atoms (C3, C4) of pyridine rings of *N*, *N*-diethylnicotinamide ligands and the oxygen atoms (O3) of *N*, *N*-diethylnicotinamide ligands of neighboring complex molecules (C3–H3A⋯O3 and C4–H4⋯O3; distances of C⋯O are in the range of 3.200–3.479 Å).

2.4. Hirshfeld Surface Analyses

Hirshfeld surface analysis was used to further study the intermolecular interactions of the crystal structures of all five compounds. For the illustrations, Figures 2 and 3 show the 3D Hirshfeld surfaces of **1** and **4**. The 3D Hirshfeld surfaces of other complexes are illustrated in the Supplementary Materials (Supplementary Figures S10–S12). The 3D Hirshfeld surfaces were mapped over the d_{norm} shape index (Figures 2 and 3, Supplementary Figures S10–S12). The surfaces are shown as transparent to allow for the visualization of the molecular moiety around which they were calculated. As shown in Supplementary Figures S10–S12, the deep red spots on the d_{norm} Hirshfeld surfaces indicate close-contact interactions, which were mainly responsible for the significant intermolecular hydrogen bonding interactions. The 3D Hirshfeld surface illustration of **1** (Figure 2), as well as of **3** (Supplementary Figure S10) and **5** (Supplementary Figure S11), shows deep red spots representing O–H⋯O hydrogen bonds. The 3D Hirshfeld surface illustration of **4** (Figure 3), as well as of **2** (Supplementary Figure S12), shows only the deep red spots that represent weak C–H⋯O hydrogen bonds. The Hirshfeld surfaces plotted over the shape index of **4** and **2** visualize the π–π stacking interactions by the presence of adjacent red and blue triangles (Figure 3, Supplementary Figure S12). The Hirshfeld 2D fingerprint of all complexes are illustrated in the Supplementary Materials (Supplementary Figures S13–S19). In the cases of **3** and **5**, which were strongly disordered, the structures are

shown separately for the main and minor part of the disorders. Hirshfeld 2D fingerprint plots allow for the quick and easy identification of significant intermolecular interactions mapped on the molecular surface [38,39]. As shown in Supplementary Figures S13–S19, strong and medium H···O/O···H hydrogen bonding interactions covered 10.3–12.7% of the total Hirshfeld surfaces with two distinct spikes in the 2D fingerprint plots, indicating the fact that hydrogen bonding interactions were the most significant interactions in the crystal structures. In the middle of the scattered points in the 2D fingerplots, H···H interactions covered 35.0–64.0% of the total Hirshfeld surfaces; however, H···H interactions were not very strong in the crystal structures. In particular, H···C/C···H interactions covered 16.5–23.7% of the total Hirshfeld surfaces in the scattered points in the 2D fingerplots. In the scattered points in the 2D fingerplots of **1–2**, H···F/F···H interactions covered 9.8–19.6% of the total Hirshfeld surfaces, and H···Cl/Cl···H interactions covered 9.4–21.1% of the total Hirshfeld surfaces for **3–4**. Furthermore, in the 2D fingerplots of **2** and **4**, significant C···C interactions are visible, covering 4.2–4.9% of the total Hirshfeld surfaces as a result of the presence of significant π–π stacking interactions in the crystal structures.
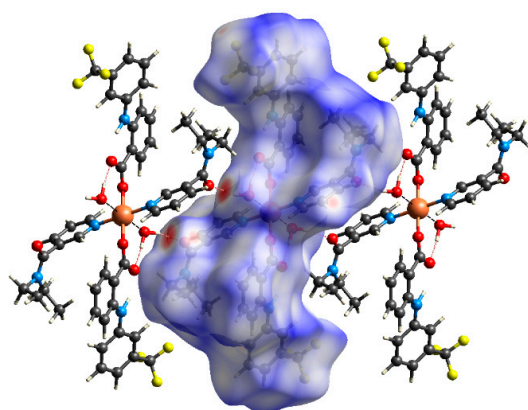
Figure 2. View of 3D Hirshfeld surface of **1** plotted over d_{norm} in the range of -0.5608 to 1.3607 a.u.
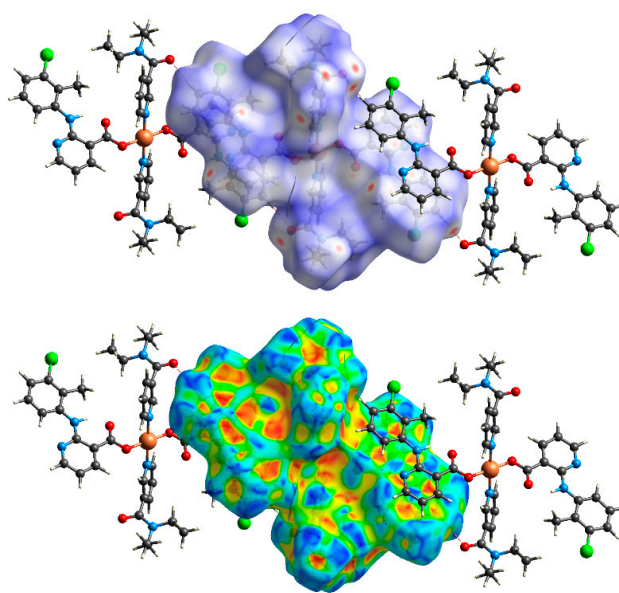
Figure 3. View of the 3D Hirshfeld surface of **4** plotted over d_{norm} in the range of -0.2000 to 1.4950 a.u. (top) and shape index (bottom).

2.5. EPR Spectroscopy

The complexes under study were investigated either as polycrystalline solids at room temperature or as frozen DMSO solutions at a low temperature (100 K). Experimental spectra were simulated using computer software in order to obtain parameters with a higher precision. The X-band EPR solid spectra of the selected complexes, **1**, **3** and **4**, are shown in Figure 4. The obtained spin Hamiltonian parameters are collected in Table 3. The EPR spectra of solid samples showed features characteristic for copper(II) monomeric complexes with S = $\frac{1}{2}$. The EPR signal was of an axial symmetry with either resolved (**3** and **4** only weakly visible) or unresolved hyperfine structures (**1**, **2** and **5**) in a parallel part of the signal as a result of the interaction of the unpaired electron with copper nuclear spin (I = 3/2) (Figure 4). The relative ordering of the axial g factors followed the usual trend ($g_\parallel > g_\perp \sim g_e$), indicating a $d_{x^2-y^2}$ ground state, which is characteristic for copper(II) atoms in tetragonally elongated octahedral arrangements around the central ion when the Jahn–Teller effect is operating. Similarly, values of the obtained g factors ($g_\perp$ = 2.055–2.082 and $g_\parallel$ = 2.29–2.36) showed only minor differences among the complexes and are in agreement with the information extracted from the crystal structures as well as from the literature for structurally similar complexes [18,27,29].
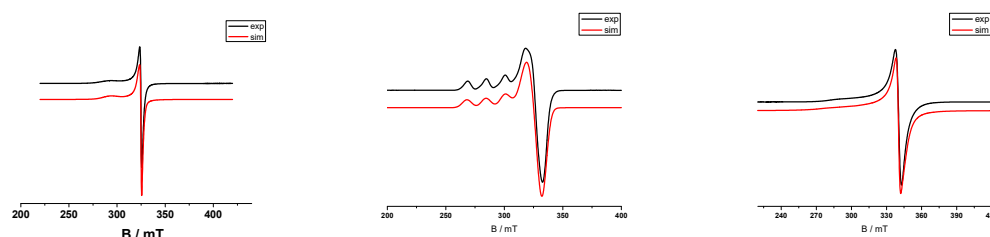
Figure 4. Room temperature solid-state spectra of **1**, **3** and **4**. Simulated spin Hamiltonian parameters are $g_\perp$ = 2.082, $g_\parallel$ = 2.290 and ΔB = (1.2, 8.5) mT (**1**); $g_\perp$ = 2.063, $g_\parallel$ = 2.305, $A_\parallel$ = 16.2 mT and ΔB = 4 mT (**3**); and $g_\perp$ = 2.055, $g_\parallel$ = 2.308, $A_\parallel$ = 16 mT and ΔB = (1.3, 8) mT (**4**).

Table 3. EPR spectral parameters of powders measured at RT and frozen DMSO solutions measured at 100 K.

Complex	Temperature	$g_\perp$	$g_\parallel$	g_{ave}	$A^{Cu}_\parallel$ /mT	G	f/cm
1	Solid RT	2.082	2.290	2.151	-	3.54	
	Sol. 100K	2.078	2.312	2.156	14.5	4.00	147
2	Solid RT	2.061	2.360	2.161	-	5.90	
	Sol. 100 K	2.077	2.303	2.152	17.5	3.94	123
3	Solid RT	2.063	2.305	2.144	16.2	4.84	132
	Sol. 100 K	2.072	2.307	2.150	16.7	4.26	128
4	Solid RT	2.057	2.308	2.140	16	5.40	134
	Sol. 100 K	2.073	2.315	2.154	15.5	4.32	138
5	Solid RT	2.055	2.320	2.143	-	5.81	
	Sol. 100 K	2.075	2.300	2.150	16.5	4.00	130

Defined as $g_{av} = (2g_\perp + g_\parallel)/3$, $G = (g_\parallel - 2)/(g_\perp - 2)$ and $f = g_\parallel/A_\parallel$.

The EPR spectra of frozen solutions are usually more informative than their analogs in a solid state due to the dilution and separation of paramagnetic ions between the neighboring molecules as a result of solvation. Because the biological measurements on the complexes were performed in the liquid phase, it was reasonable to have the solution EPR spectra to obtain more appropriate structural information for correlating the experimental results. The EPR spectra of DMSO solutions measured at 100 K are depicted in Figure 5 (for selected complexes **1**, **4** and **5**).
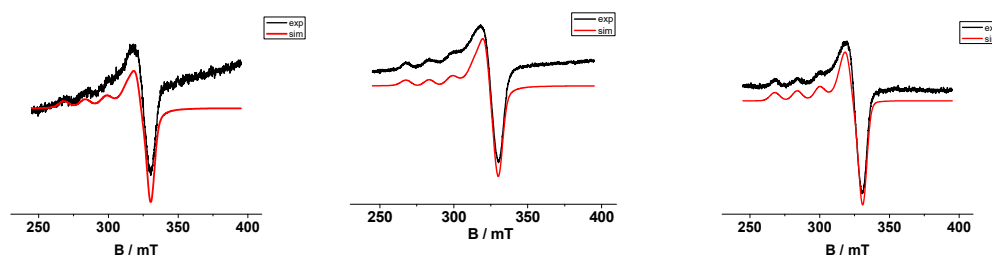
Figure 5. EPR spectra of **1**, **4** and **5** measured in DMSO solutions at 77K. Simulated spin Hamiltonian parameters are $g_\perp$ = 2.078, $g_\parallel$ = 2.312, $A_{||}$ = 14.5 mT and ΔB = 3.5 mT; $g_\perp$ = 2.073, $g_\parallel$ = 2.315, $A_\parallel$ = 15.5 mT and ΔB = (2.8, 3.5) mT; and $g_\perp$ = 2.075, $g_\parallel$ = 2.300, $A_\parallel$ = 16.5 mT and ΔB = 3 mT.

For all five complexes, the EPR spectra of frozen DMSO solutions showed axial symmetry with resolved parallel hyperfine splitting showing a tree of four peaks. The spin Hamiltonian parameters obtained from the EPR simulations are collected in Table 3. The obtained EPR data show a close resemblance ($g_\perp$ = 2.072–2.078, $g_\parallel$ = 2.300–2.315, $A_\parallel$ = 14.5–17.5 mT) as a result of the similar structures of complexes in DMSO solutions. This fact can be clearly seen when looking at the alike values of the derived EPR parameters, such as g_{ave}, G or $g_\parallel / A_\parallel$, are also summarized in Table 3. The values of the geometric parameters G were very close to 4.00, indicating that the complexes exhibit minimal exchange interactions between copper(II) centers [35]. Similarly, values of the parameter of the tetrahedral distortion $f = g_\parallel / A_\parallel$ ranged from 123 cm for **2** to 147 cm for **1** between the studied complexes. Such values indicate that only minor tetrahedral distortion around the central copper ion existed in the primary coordination sphere, in accordance with the crystallographic information [40]. We can conclude that the observed similarity among the solid and solution EPR data suggest a close similarity in the geometries of the studied complexes.

2.6. SOD Mimetic Activity

The SOD mimetic activity of the studied complexes was characterized via an NBT assay. The superoxide radical was generated with xanthine and a xanthine oxidase biochemical system, and the ability of the complexes to scavenge the superoxide was tested indirectly via the reduction of NBT dye. Colour changes in NBT were detected at 560 nm. When the potential scavenging complex was added to the system, a competing reaction between the complex and superoxide would occur, which led to the inhibition of the reaction between NBT and the superoxide. The scavenging activity of the studied complexes was evaluated and characterized with the IC_{50} value (Figure 6).
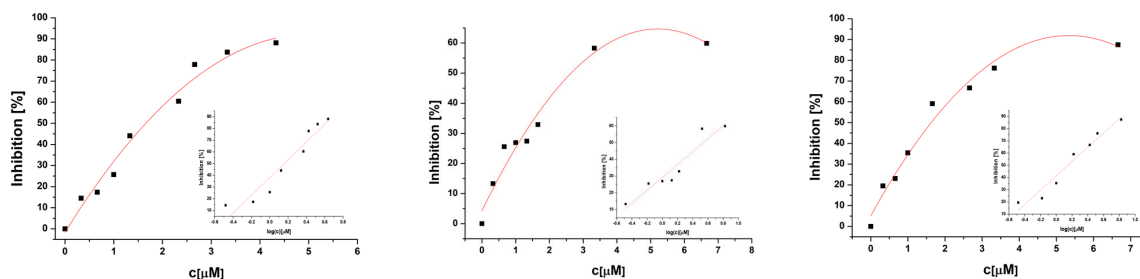
Figure 6. SOD mimetic activity of **2**, **3** and **4**.

The inhibition concentration IC_{50} corresponds to the concentration of the complex that caused 50% inhibition of the NBT reduction. The results are collected in Table 4. The complexes showed significant SOD-like activity, comparable to the SOD mimetic activity of other copper fenamates [3,27,41,42]. Complexes **2** and **4** exhibited the greatest radical scavenging effect with micromolar concentrations. On the basis of these results, the complexes could be considered as the good SOD mimetics [3].

Table 4. SOD mimetic activity of selected copper NSAIDs.

Complex	$IC_{50}/\mu M$	Reference
$[Cu(fluf)_2(dena)_2(H_2O)_2]$ (**1**)	3.33	This work
$[Cu(nifl)_2(dena)_2]$ (**2**)	1.69	This work
$[Cu(tolf)_2(dena)_2(H_2O)_2]$ (**3**)	3.46	This work
$[Cu(clon)_2(dena)_2]$ (**4**)	1.41	This work
$[Cu(mef)_2(dena)_2(H_2O)_2]$ (**5**)	3.15	This work
$[Cu(tolf)_2(phen)]$	0.98	[27]
$[Cu(mef)_2(phen)]$	1.23	[27]
$[Cu(fluf)_2(phen)]$	0.94	[27]
$[Cu(3\text{-mesal})_2(dena)_2(H_2O)_2]$	3.88	[41]
$[Cu(tolf)_2(H_2O)]_2$	1.97	[42]
Native SOD	0.04	[3]

2.7. Interactions of Complexes with KO_2 in the Presence of Neocuproine

The first step in the mechanism of action of native CuZn-SOD enzymes is the binding of the superoxide radical anion to the copper center, where Cu(II) is subsequently reduced to Cu(I) and the oxygen molecule is released [43]. Therefore, the ability of the prepared complexes to undergo reduction with the superoxide radical anion is an important step in the investigation of their potential SOD activity. To verify this assumption, we used a specific Cu(I) chelator, neocuproine, which forms a stable Cu(I)-neocuproine complex that absorbs at 458 nm [44]. The addition of potassium superoxide (KO_2) to the solutions of complexes **1–4** in the presence of neocuproine resulted in a dramatic increase in absorbance at 458 nm for complexes **1–4** and a visible reduction in the d-d band intensity of the studied complexes, as can be clearly seen in Figure 7. Thus, from these results we can assume that the prepared complexes **1–4** undergo reduction to Cu(I) under the influence of KO_2 and thus fulfill an important prerequisite to be good SOD mimetics.
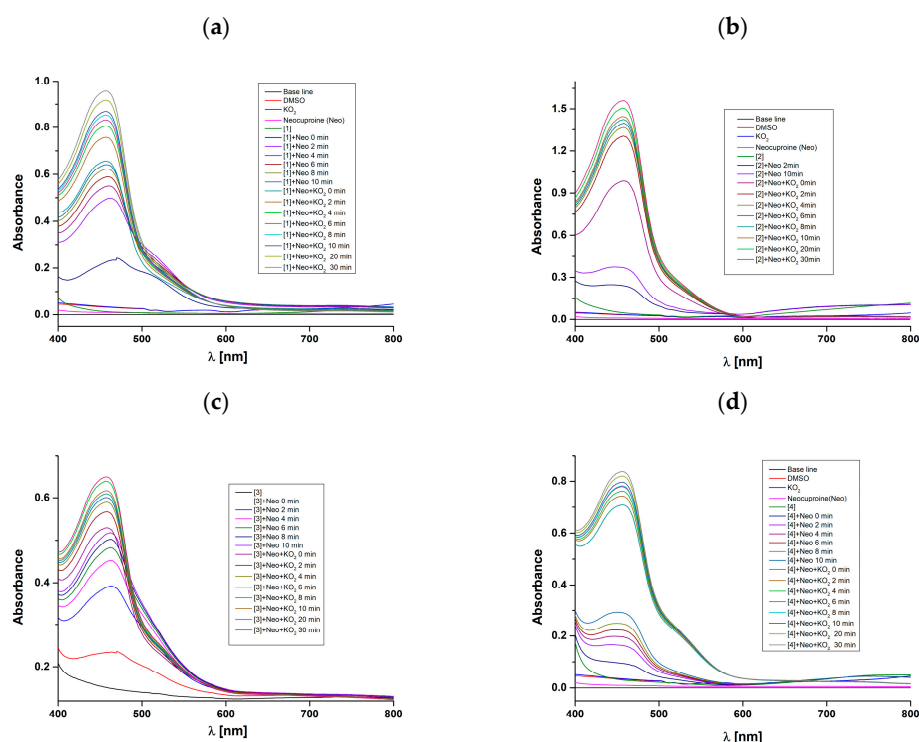
Figure 7. Time-dependent UV-Vis spectra of the interaction of studied complexes and KO_2 in DMSO in the presence of neocuproine: (**a**) **1**; (**b**) **2**; (**c**) **3**; (**d**) **4**.

2.8. Cyclic Voltammetry

The redox behavior of the studied complexes (prepared in DMSO) was investigated by means of cyclic voltammetry using a scan rate of 100 mV/s. Figure 8 displays the cyclic voltammograms of corresponding complexes **1–5** at a concentration level of 10^{-4} M, which were registered in the presence of 0.1 M NaCl as a supporting electrolyte at the boron-doped diamond (BDD) electrode. A summary of the basic redox parameters for the studied complexes are listed in the Table 5. In the cyclic voltammetric records, two potential regions were differentiated. In the first potential region between −0.136 V and −0.085 V, Cu(II)/Cu(I)-based redox transitions were observed, which showed better resolved peak currents in the anodic scan, with $E_{p,ox}$ ranging from −0.136 V (**4**) to −0.124 V (**3**). In the cathodic scan, the corresponding reduction waves could be identified at a peak potential ranging from −0.097 V (**3**) to −0.083 V (**1**). The observation of both potentials for all studied complexes indicated the quasi-reversible redox process undertaken at the BDD electrode. The same conclusion could be read from values of the $I_{p,ox}/I_{p,red}$ ratio, and the value of this ratio ranged from the lowest value of 1.3 for **3** to the highest of 2.1 for **4**. In the second potential region, quite distinctive voltammetric curves with oxidation peak potentials ranging from 0.633 V (**5**) to 0.941 V (**2**) could be noticed, which may be attributed to the redox activity within the bis(fenamate) ligand. Finally, to be good SOD mimetics, the redox potential ($E°$ vs. Ag/AgCl) should fall between −0.363 V and +0.687 V, as in the case of a native SOD enzyme [27]. This criterion was succesfully fulfilled for all studied complexes according their $E_{1/2}$ values (Table 5).
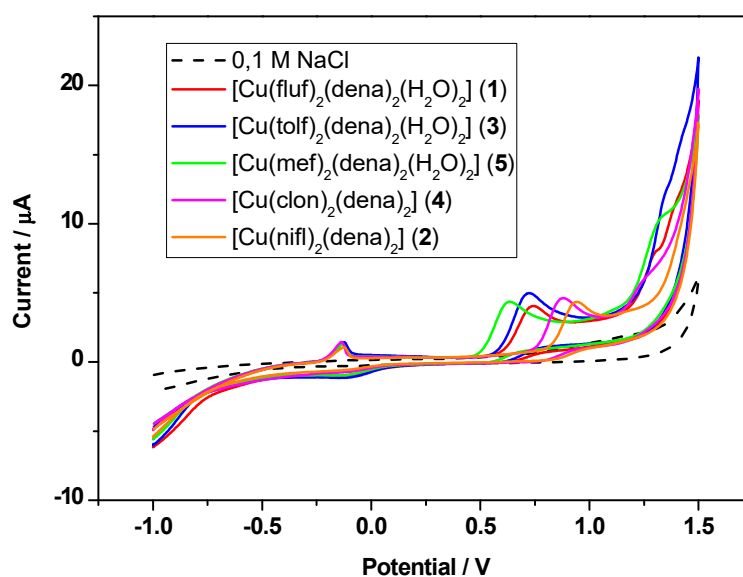
Figure 8. Cyclic voltammograms of **1–5** (c(complex) = 10^{-4} M) in 0.1 M NaCl measured at BDD electrode using scan rate of 100 mV/s.

Table 5. Redox parameters of **1–5** extracted from experimental CV data.

Comp	$E_{p,ox}$/V	$E_{p,red}$/V	$E_{1/2}$/V	ΔE/V	$I_{p,ox}$/µA	$I_{p,red}$/µA	$E_{p,ox}$/V	$I_{p,ox}$/µA
1	−0.133	−0.085	−0.109	−0.048	1.386	−0.917	0.741	4.05
2	−0.126	−0.096	−0.111	−0.030	1.064	−0.542	0.941	4.36
3	−0.124	−0.097	−0.111	−0.027	1.427	−1.104	0.734	5.00
4	−0.136	−0.096	−0.116	−0.040	1.449	−0.681	0.877	4.62
5	−0.133	−0.087	−0.110	−0.046	1.279	−0.876	0.633	4.36

2.9. ct-DNA Interaction Studies

Transition metal complexes, such as copper complexes, can bind to DNA and thus induce DNA cleavage, which can be exploited in the preparation of DNA structural probes, cleavage or anticacer agents [45]. Moreover, if complexes contain ligands with suitable functional groups that can be involved in hydrogen bonding or in electrostatic, hydrophilic/hydrophobic or $\pi-\pi$ stacking interactions, then they can be rationally utilized to support the binding abilities of complexes toward the DNA [46]. Copper complexes can interact with DNA either covalently through the formation of covalent adducts (e.g., cis-platin) or non-covalently [47]. The non-covalent mode of binding between complexes and DNA includes intercalation (using mostly $\pi-\pi$ stacking interactions), groove binding (van der Waals interactions or hydrogen bonding) and external binding (electrostatic interactions) [48]. Interactions of the prepared complexes **1–4** with calf thymus DNA were evaluated using UV-Vis absorption titrations and viscosity measurements, as well as with fluorescence emission with an ethidium bromide (EB) displacement method.

2.9.1. Absorption Titrations

The absorption spectra of the DMSO/buffer solutions of the studied complexes **1–4** exhibited a very similar pattern of absorption bands in the UV region from 250 nm to 400 nm (Figure 9). Two types of signals existed in the UV spectrum, which has different behavior upon the addition of DNA. First, for tree absorption bands with maxima located at 255, 262 and 269 nm, a sudden decrease in absorption was observed after the addition of the first amount of DNA. Then, the further addition of DNA led to band hyperchromism. Because the positions of the bands did not move after the addition of DNA, we assumed that the increase in absorbance was due to the further addition of DNA with an absorption band in this part of spectra (at 260 nm). Two other absorption peaks, coming from intraligand π to π^* transitions of aromatic NSAID moieties at around 280 nm (high-intensity discrete peak) and 320 nm (lower-intensity shoulder), showed a considerable decrease in the absorption of complexes (11.8% for **2** to 21.4% for **1**) together with a slight blue shift (1–5 nm) (Table 6). A hypochromic shift is usually associated with the stabilization of DNA secondary structures via electrostatic interactions or the intercalation of metal complexes [46,48]. The observed hypochromism and blue shift thus suggest an electrostatic or intercalative binding mode of complex–DNA interactions or their combination. However, as reported, absorption titrations give only preliminary information about complex–DNA interactions, and therefore, further measurements are necessary to clarify the binding mode [26]. The internal DNA binding K_b constants of **1–4** were determined using the most intensive and best resolved band at 288 nm with the Wolfe–Shimmer equation (inset in Figure 9).

The values of the K_b binding constants are collected in the Table 6. The obtained values of the K_b constants ranged from 1.04×10^5 (**2**) to 5.46×10^5 M^{-1} (**4**) and are in good agreement with other Cu–fenamate complexes [23,27–30]. Such values indicate relatively strong binding of the studied complexes to DNA, likely due to their ability to form hydrogen bonds with DNA in combination with partial intercalation. Based on their binding strength with DNA, the complexes can be arranged as follows: **4 > 1 > 3 > 2**. The highest values of the binding constant were obtained for complexes with clonixinate and flufenamate ligands (5.46×10^5 M^{-1} and 4.83×10^5 M^{-1}, respectively). Based on these values, there seemed to be no apparent structural trend between structurally similar complexes **2, 4** vs. **1, 3** with respect to the planarity of complexes **2** and **4**. Instead, the combined effect of electrostatic interactions, which is stronger for **1**, and intercalation through coplanar pyridine and benzene rings, which prefer complex **4**, could be operative. However, as was noticed, the exact mode of binding of the complexes into DNA cannot be determined using only absorption titration studies, so further measurements are necessary to confirm the obtained results [24–27].
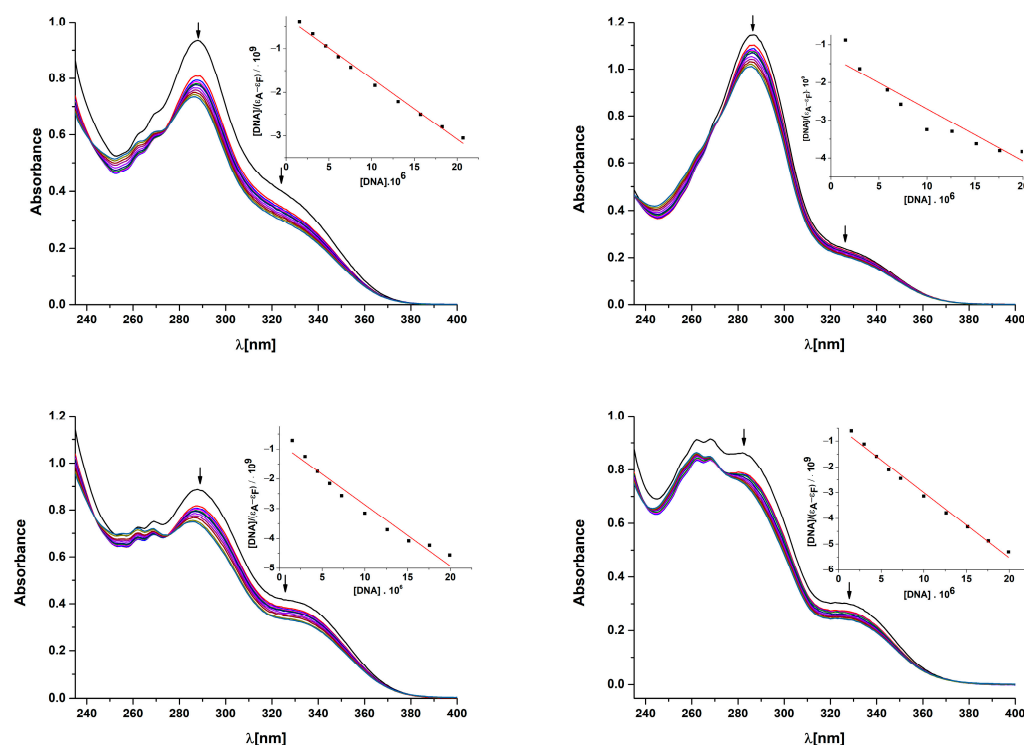
Figure 9. UV-Vis spectra of DMSO/buffer solution of **1**–**4** in the absence and presence of increasing amounts of DNA (*r* = [DNA]/[complex] = 0–2.1). Arrows show changes in intensity upon the addition of increasing amounts of DNA. Inset: Plot of [DNA]/(ε_A-ε_f) versus [DNA] for complex.

Table 6. DNA binding constant and UV spectral features of **1**–**4** in the presence of DNA.

Complex	K_b [M^{-1}]	R^2	λ(nm)($\Delta A/A_0$ (%), $\Delta\lambda$ * (nm)
[Cu(fluf)$_2$(dena)$_2$(H$_2$O)$_2$] (**1**)	4.83 ($\pm$0.84) · 10^5	0.9897	287(21.4, −1)
[Cu(nifl)$_2$(dena)$_2$] (**2**)	1.04 ($\pm$0.75) · 10^5	0.8699	287(11.8, −2)
[Cu(tolf)$_2$(dena)$_2$(H$_2$O)$_2$] (**3**)	2.52 ($\pm$0.87) · 10^5	0.9551	288(15.7, −3)
[Cu(clon)$_2$(dena)$_2$] (**4**)	5.46 ($\pm$0.87) · 10^5	0.9906	281(12,3, −5)

* denotes blue shift.

2.9.2. Viscosity Measurements

Because DNA viscosity manifests sensitivity to DNA length changes in the presence of a DNA binder, it was desirable to carry out the DNA viscosity measurements in the presence of complexes with potential binding activity [48]. The DNA viscosity measurements were performed on DNA solutions in the presence of increasing concentrations of complexes **1**–**4**. In addition, the planar molecule of ethidium bromide (EB), which is known as a perfect nonspecific DNA intercalating agent, was used as an indicator of intercalation. As is clearly seen in Figure 10, in the presence of growing concentrations of complexes, a continual increase in the relative DNA viscosity for all four complexes was observed. This behavior supports the hypothesis about the intercalative interaction between the complex molecules and DNA. The results reveal that the best intercalating ability in this series had a complex with the flufenamate ligand (**1**). On the other hand, the relative DNA viscosity of the complex with clonixinate (**4**) gave, in this case, the lowest increase in the studied series (**1** > **2** $\approx$ **3** > **4**). A comparison with an EB molecule suggests that the studied complexes were weaker intercalating agents than EB, but it can be noted that all four complexes could bind to DNA via partial intercalation. Finally, no apparent trend between structurally similar complexes **2**, **4** vs. **1**, **3** was visible.
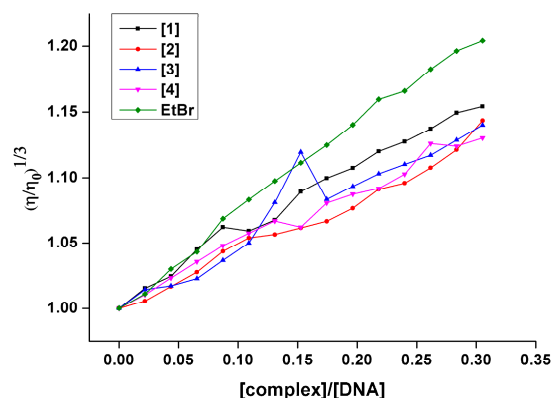
Figure 10. Relative viscosity of DNA in the buffer solution in the presence of studied complexes (**1–4**) under the condition of increasing the concentration ratio [complex]/DNA.

2.9.3. Competitive Studies with EB-DNA

Another method that was used to investigate the intercalating ability of complexes to DNA was a competitive study of the DNA interactions of the complexes with the ethidium bromide (EB) displacement method. EB represents a typical DNA intercalator that intercalates into DNA, and at the same time, it is a very effective fluorophore in the presence of DNA. When EB interacts with DNA, it creates an EB-DNA adduct that emits an intense fluorescence emission band at 615 nm when excited at 540 nm. The addition of a complex with an affinity to DNA lowers the emission intensity of the EB adduct due to competition with EB at the same binding sites in DNA. The representative fluorescence emission spectra of **4** are shown in Figure 11. The addition of increased concentrations of complexes led to a decrease in the intensity of the emission band of the EB-DNA adduct at 615 nm. The final quenching of the fluorescence reached 30–35% of the initial EB-DNA fluorescence intensity (Figure 11). Very similar results of quenching with copper fenamates were also observed by other authors [21]. The observed moderate decrease in EB-DNA fluorescence emission in the presence of complexes indicates their competitive binding ability when compared with EB. The quenching of EB bound to DNA is in good accordance with the linear Stern–Volmer equation, thus providing further proof of the observed DNA-binding ability of the studied complexes. The calculated values of the K_{sv} constant (3.30–3.79 $\times$ 10^3 M^{-1}) confirmed the moderate intercalative ability of the complexes towards DNA (Table 7) when comparing these values with other copper fenamates, which show values of K_{sv} 10^5–10^6 [22,26,29]. In addition, the calculated values of the EB-DNA quenching rate constant k_q of order 10^{11} M^{-1} s^{-1} (Table 7) suggest the presence of a static quenching mechanism (k_q > 10^{11} M^{-1} s^{-1}) [5].
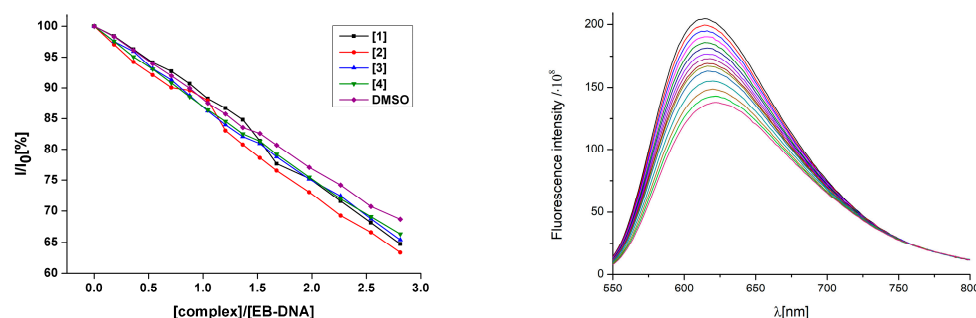
Figure 11. Graphical dependence of relative EB-DNA fluorescence emission intensity (I/I$_0$) at 615 nm vs. concentration ratio [complex]/DNA for **1–4**. Fluorescence emission spectra for EB-DNA in the buffer solution in the presence of increasing amounts of **4**.

Table 7. EB-DNA fluorescence (%), calculated Stern–Volmer constant K_{SV} and the quenching rate constant k_q of DMSO and complexes **1–4**.

Complex	$\Delta I/I_0$ (%)	K_{sv} (M^{-1})/10^3	k_q (M^{-1} s^{-1})/10^{11}
[Cu(fluf)$_2$(dena)$_2$(H$_2$O)$_2$] (**1**)	35.2	3.59 ($\pm$0.16)	1.56 ($\pm$0.07)
[Cu(nifl)$_2$(dena)$_2$] (**2**)	36.7	3.79 ($\pm$0.13)	1.65 ($\pm$0.06)
[Cu(tolf)$_2$(dena)$_2$(H$_2$O)$_2$] (**3**)	31.2	3.40 ($\pm$0.09)	1.48 ($\pm$0.04)
[Cu(clon)$_2$(dena)$_2$] (**4**)	33.6	3.30 ($\pm$0.08)	1.44 ($\pm$0.04)
DMSO	30.9	3.03 ($\pm$0.07)	1.32 ($\pm$0.03)

2.10. Interaction of Studied Complexes with BSA

The fluorescence emission spectra of bovine serum albumin showed intense fluorescence emission at 336 nm due to the existence of two tryptophan moieties at positions 134 and 212. The interaction of complexes **1–4** with bovine serum albumin was studied by monitoring spectral changes in tryptophan fluorescence emission after the addition of complexes [49]. The graphical dependence of the relative BSA fluorescence intensity on increasing amounts of complexes **1–4** showed significant quenching of the fluorescence up to 89–91% for all studied complexes (Figure 12).

(a)   **(b)**
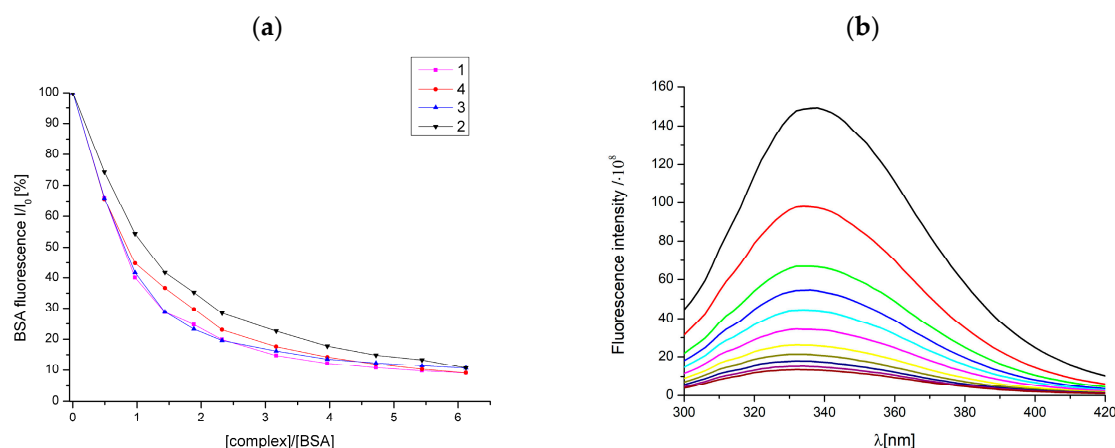
Figure 12. (**a**) Graphical dependence of relative BSA fluorescence intensity in % at λ = 336 nm vs. concentration ratio [complex]/BSA. (**b**) Fluorescence emission spectra for EB-DNA in the buffer solution in the presence of increasing amounts of **4**.

These results confirm the fact that the complexes were able to bind to serum albumin in significant amounts, likely through tryptophan residue. In addition, the interaction of complexes with serum albumin was characterized with the Stern–Volmer constant K_{sv} and the quenching constant k_q, which was calculated using the Stern–Volmer equation. Furthermore, the association binding constant K_{BSA} and the number of binding sites per albumin n, were determined using the Scatchard equation as well (Supplementary Figure S20). The obtained values are summarized in Table 8. The values of the K_{sv} constants of order 4–5×10^5 M^{-1} indicate an intermediate binding strength between the complexes and albumin. The presented values of the quenching constant k_q of order 10^{13} are much larger than 10^{10} M^{-1} s^{-1}, which represents a typical value for a quencher used in biopolymer quenchers. High values also indicate that quenching is performed through the static quenching mechanism [21,28]. The highest quenching ability was observed for complexes **1** and **4** according to their k_q values. As reported, the optimal range assumed for a serum albumin drug delivery system (capable of providing adequate transport and distribution in the bloodstream and reversible release of the drug to the target) should have K_{sv} values in the range of 10^2–10^8 M^{-1} and K_{BSA} values in the range of 10^4–10^6 M^{-1} [49]. The calculated values of K_{sv} and K_{BSA} for the studied complexes **1–4** are within the optimal range.

Table 8. Values of the Stern–Volmer quenching constant (K_{sv}), quenching constant (k_q), association binding constant (K_{BSA}) and n (number of binding sites for albumin) obtained for the interaction of **1–4** with bovine serum albumin.

Complex	K_{sv} (M^{-1})/10^5	k_q (M^{-1} s^{-1})/10^{13}	K_{BSA} (M^{-1})/10^5	n
[Cu(fluf)$_2$(dena)$_2$(H$_2$O)$_2$] (**1**)	5.777	2.51 ($\pm$0.061)	3.39 ($\pm$0.413)	1.11
[Cu(nifl)$_2$(dena)$_2$] (**2**)	4.411	1.92 ($\pm$0.073)	2.18 ($\pm$0.164)	1.16
[Cu(tolf)$_2$(dena)$_2$(H$_2$O)$_2$] (**3**)	4.740	2.06 ($\pm$0.092)	3.36 ($\pm$0.417)	1.10
[Cu(clon)$_2$(dena)$_2$] (**4**)	5.558	2.42 ($\pm$0.054)	3.32 ($\pm$0.147)	1.08

2.11. Anticancer Activity

Copper complexes **1–4** were tested for their in vitro cytotoxicity against three cancer cell lines, including human lung cancer cells (A549), human breast cancer cells (MCF-7), human glioblastoma cells (U-118MG) and a healthy human lung fibroblast cell line (MRC-5), respectively. The cells (8×10^3 cells/200 µL well) were treated with several concentrations (20–100 µmol/L) of **1–4** for 24, 48 and 72 h, and the cytotoxicity was evaluated using an MTT assay. The measurement was repeated twice using three parallels for each concentration. The inhibitory concentration values (IC_{50}) of the studied complexes for the A549 and U-118MG cancer cell lines were higher than the highest concentration used of 100 µM at each incubation time (data not shown). In the case of the MCF-7 tumor cell line, the same results were obtained for complexes **1–3** ($IC_{50} > 100$ µM). On the other hand, complex **4** showed cytotoxicity against MCF-7 cells after 72 h of exposure with an IC_{50} value of 57 ± 3 µM. As can be seen from the graph (Figure 13a), the viability of the MCF-7 tumor cells decreased with increasing concentrations of **4** for 72 h of exposure. In addition, no cytotoxic effect was observed on healthy MRC-5 cells for 72 h of incubation under the same conditions (Figure 13b).
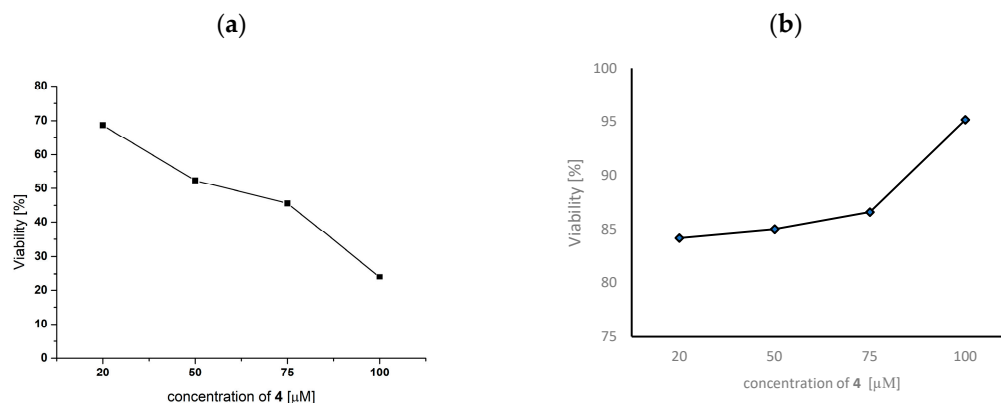
Figure 13. Cell proliferation of (**a**) MCF-7 cancer cells and (**b**) MRC-5 healthy cells in response to **4** after 72 h of exposure. Cell lines were treated (20–100 µmol/L) with complex **4**, and viable cells were evaluated using a colorimetric assay.

Complex **4** contains the ligand clonixin in its structure, which has antipyretic, antianalgesic and antirheumatic effects, and especially anti-inflammatory effects [50]. The antitumor effects of clonixin alone or of copper complexes with clonixin have not been described so far. However, some authors have focused on the effect of clonixin with platinum, as the anti-inflammatory strategy is key in the treatment of aggressive cancer diseases [51]. They investigated a platinum (IV) prodrug complex with NSAIDs (non-steroidal anti-inflammatory drugs) as ligands designed to effectively enter tumor cells due to their high lipophilicity, where they can release a cytotoxic metabolite [51]. This mechanism reduces side effects and increases the therapeutic efficacy of the drug used in chemotherapy. Copper(II) complexes containing coordinated clonixin seem to be a potential metallo-drug for closer follow-up of its biological effects, as we did not observe a

cytotoxic effect on healthy MRC-5 cells for 72 h of incubation under the same conditions (Figure 13b). In addition, copper complexes with tolfenamic, mefenamic and flufenamic acids and phenanthroline can have anti-tumor effects [27]. The authors confirmed the effect of these substances according to their ability to generate intracellular reactive oxygen species (ROS) and inhibit cyclooxygenase-2 (COX-2), an enzyme that is overexpressed in breast tumors. They detected DNA damage, JNK and p38 pathway activation and an apoptosis pathway [27].

In the second step of our biological research, we were interested in the genotoxic effect of the selected copper complexes. Considering that complexes **1–3** did not show any cytotoxic activity for 72 h of incubation with A549, U-118MG and MCF-7 tumor cells in the concentration range (20–100 μmol/L), we chose complex **4** with an IC_{50} of $57 \times$ μM. We affected MCF-7 cells with the IC_{50} value and monitored DNA damage after 72 h of incubation. Unfortunately, we did not observe any significant DNA damage compared to control cells, which were not affected by **4** (Figure 14). The DNA damage did not exceed a threshold of 10%, which is considered relevant DNA damage.
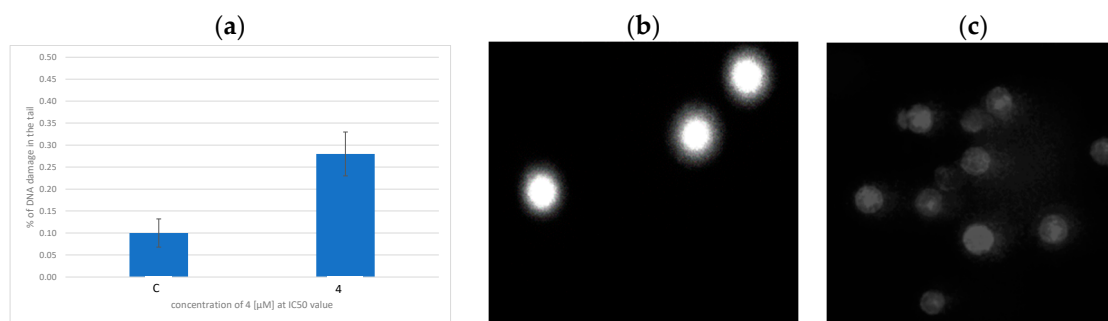
Figure 14. (**a**) Analysis of DNA damage of MCF-7 cells treated with **4**. Morphology of (**b**) control (cells were not treated) and (**c**) damaged MCF-7 cells treated with **4** at an IC_{50} of 57 ± 3 μM.

3. Materials and Methods

General procedures. All reagents and solvents were obtained from commercial sources and used as received unless noted otherwise.

3.1. Synthesis

[Cu(fluf)$_2$(dena)$_2$(H$_2$O)$_2$] (1)

Complex **1** was prepared with the following procedure. Copper acetate dihydrate (1 mmol, 0.170 g) was dissolved in 30 mL of ethanol. Then, sodium flufenamate, formed in situ by mixing an equimolar amount of flufenamic acid (2 mmol, 0.564 g) with sodium hydroxide (2 mmol, 0.080 g), was slowly poured into the solution. The solution immediately changed color from blue-green to green. After 10 min, *N*, *N*-diethylnicotinamide (2 mmol, 0.356 g, 0.4 mL) was added dropwise to form a clear dark green solution. After a while, a dark green precipitate was formed. Afterward, the mixture was stirred for 3 h at room temperature, before the crude product was filtered through smooth filtration paper and dried in the air. The pale green needle-like crystals of **1** suitable for crystallographic analyses were isolated from the mother liquor after a week.

Yield: 0.71 g (70%). Anal. calc. for C$_{48}$H$_{50}$CuF$_6$N$_6$O$_8$ (M_r = 1016.504): C 57.29, H 4.93, N 8.70 %. Found: C 56.72, H 4.96, N 8.27 %. IR (ATR, cm^{-1}): 3507 (m), 3324 (w), 3218 (w), 3091 (m), 2979 (m), 2934 (w), 1619 (s), 1606 (s), 1581 (s), 1568 (s), 1499 (s), 1456 (s), 1421 (ms), 1378 (vs), 1331 (vs), 1284 (s), 1183 (ms), 1159 (ms), 1109 (vs), 1069 (s), 1046 (ms), 997 (m), 930 (m), 872 (m), 826 (m), 753 (s), 697 (s), 650 (m). UV-Vis: λ / nm (ε/M^{-1}cm^{-1}) as nujol mulls (nm): 210, 234 (sh), 287 (sh), 322 (sh), 412 (sh), 646; in DMSO / H$_2$O: 255 (35440), 262 (40030), 269 (44900), 287 (62300), 320 (28300, sh), 795 (65).

[Cu(nifl)$_2$(dena)$_2$] (2)

Complex **2** was prepared with the same procedure used for complex **1**. Violet prismatic crystals suitable for X-ray analysis formed after a week.

Yield: 0.56 g (57%). Anal. calc. for $C_{48}H_{44}CuF_6N_8O_6$ (M_r = 982.448): C 57.05, H 4.70, N 11.83 %. Found: C 56.24, H 4.51, N 11.41 %. IR (ATR, cm^{-1}): 3269 (w), 3163 (w), 3117 (w), 2979 (m), 2936 (w), 2874 (w), 1629 (s), 1595 (vs), 1582 (vs), 1518 (s), 1494 (s), 1456 (s), 1420 (ms), 1387 (s), 1368 (s), 1324 (vs), 1293 (sh), 1160 (s), 1115 (s), 1096 (s), 1067 (s), 997 (w), 943 (m), 869 (m), 826 (m), 783 (s), 699 (s), 670 (m),471 (m), 413 (m). UV-Vis: λ/nm (ε/M^{-1}cm^{-1}) as nujol mulls (nm): 203 (sh), 286, 343 (sh), 412 (sh), 539 (br); in DMSO/H_2O: 262 (36270), 269 (46000), 287 (68950), 320 (14830, sh), 791 (95).

[Cu(tolf)$_2$(dena)$_2$(H$_2$O)$_2$] (3)

Dark green crystals of **3** suitable for X-ray analysis were isolated after two weeks.

Yield: 0.69 g (75%). Anal. calc. for $C_{48}H_{54}Cl_2CuN_6O_8$ (M_r = 977.450): C 59.70, H 5.86, N 9.82 %. Found: C 58.98, H 5.57, N 8.60 %. IR (ATR, cm^{-1}): 3458 (m), 3206 (m, br), 3094 (m), 2992 (m), 2938 (w), 1613 (s), 1579 (s), 1557 (s), 1493 (s), 1442 (s), 1377 (vs), 1281 (s), 1186 (m), 1107 (m), 1008 (m), 947 (m), 879 (m), 831 (m), 758 (s), 736 (s), 699 (s), 636 (m), 528 (m), 416 (m). UV-Vis: λ/nm (ε/M^{-1}cm^{-1}) as nujol mulls (nm): 221 (sh), 246 (sh), 294 (sh), 338 (sh), 412 (sh), 628 (br); in DMSO/H_2O: 255 (20820), 261 (21550), 269 (22550), 288 (26660), 325 (12520, sh), 789 (230).

[Cu(clon)$_2$(dena)$_2$] (4)

Complex **4** was prepared with the same procedure used for complex **1,** with the exception of the used solvent, which was, in this case, methanol. Brown prismatic crystals suitable for X-ray analysis formed after a week.

Yield: 0.68 g (72%). Anal. calc. for $C_{46}H_{48}Cl_2CuN_8O_6$ (M_r = 943.395): C 59.56, H 5.07, N 11.93 %. Found: C 58.56, H 5.13, N 11.88 %. IR (ATR, cm^{-1}): 3275 (w), 3186 (w), 3114 (w), 3066 (w), 2980 (w), 2937 (w), 1629 (s), 1602 (s), 1585 (s), 1519 (s), 1456 (s), 1434 (ms), 1380 (m), 1358 (s), 1315 (vs), 1256 (ms), 1189 (m), 1101 (m), 1015 (m), 924 (m), 880 (w), 823 (m), 766 (vs), 702 (s), 653 (m), 536 (m), 414 (m). UV-Vis: λ/nm (ε/M^{-1}cm^{-1}) as nujol mulls (nm): 224 (sh), 298, 340 (sh), 419 (sh), 529 (br), 629 (sh); in DMSO/H_2O: 262 (54960), 268 (55100), 281 (51900), 320 (18170, sh), 794 (116).

[Cu(mef)$_2$(dena)$_2$(H$_2$O)$_2$] (5).

Complex **5** was prepared as described for **1**. Dark green crystals of **5** suitable for X-ray analysis were obtained after two weeks.

Yield: 0.58 g (62%). Anal. calc. for $C_{50}H_{60}CuN_6O_8$ (M_r = 936.615): C 65.89, H 6.17, N 9.16 %. Found: C 65.38, H 6.36, N 9.15 %. IR (ATR, cm^{-1}): 3473 (w), 3217 (w, br), 2991 (w), 2934 (w), 1612 (s), 1575 (s), 1561 (s), 1496 (s), 1449 (s), 1376 (s), 1281 (s), 1214 (m), 1186 (m), 1105 (m), 947 (w), 920 (w), 878 (w), 831 (m), 783 (m), 760 (s),739 (m), 699 (m), 636 (m), 530 (m), 415 (m). UV-Vis: λ/nm (ε/M^{-1}cm^{-1}) as nujol mulls (nm): 216 (sh), 268 (sh), 346, 407 (sh), 600 (br); in DMSO/H_2O: 288 (22420), 330 (sh, 11400), 801 (56).

3.2. Physical Measurements

Carbon, hydrogen and nitrogen analyses were carried out on a CHNSO FlashEA^{TM} 1112 Automatic Elemental Analyzer. The electronic spectra (190–1100 nm) of the complexes were measured in a Nujol suspension with a SPECORD 250 Plus (Carl Zeiss Jena) spectrophotometer at room temperature. The infrared spectra (ATR technique, 4000–400 cm^{-1}) were recorded on a Nicolet 5700 FT-IR spectrophotometer at room temperature. Room-temperature EPR spectra of the powdered samples were recorded with an EPR spectrometer EMX Plus series (Bruker, Germany) operating at X-band ($\approx$9.4 GHz) and simulated using Spin.exe software developed by Dr. Ozarowski [52].

3.3. X-ray Crystallography

The data collection and cell refinement of **1–5** were carried out using the four-circle diffractometer Stoe StadiVari using the Pilatus3R 300K HPD detector and the microfocused X-ray source Xenocs Genix3D Cu HF (Cu Kα radiation). The diffraction intensities were corrected for Lorentz and polarization factors. The absorption corrections were made with

the LANA program [53]. The structures were solved using the ShelXT [54], Superflip [55] or Sir14 [56] program and refined using the full-matrix least-squares procedure of the Independent Atom Model (IAM) with ShelXL (version 2018/3) [57]. Hirshfeld Atom Refinement (HAR) was carried out using the IAM model as a starting point. The wave function was calculated using ORCA 4.2.0 software [58] with the basis set jorge-TZP [59] and hybrid exchange–correlation functional PBE0 [60]. The least-squares refinements of the HAR model were then carried out with olex2.refine (version 1.5) [61], while keeping the same constraints and restraints as those used for the ShelXL refinement. The NoSpherA2 implementation [62] of HAR is used for tailor-made aspherical atomic factors calculated on-the-fly from a Hirshfeld-partitioned electron density. For the HAR approach, all H atoms were refined isotropically and independently. All calculations and structure drawings were performed in the OLEX2 package [63]. Ortep-like representations of the independent part of the crystal structures of **1–5** are shown in Supplementary Figures S3–S7. The crystal data and parameters of structure refinement are listed in Table 9.

Table 9. Crystallographic data for compounds **1–5**.

	1	2	3	4	5
Chemical formula	$C_{48}H_{50}CuF_6N_6O_8$	$C_{48}H_{44}CuF_6N_8O_6$	$C_{48}H_{54}Cl_2CuN_6O_8$	$C_{46}H_{48}Cl_2CuN_8O_6$	$C_{50}H_{60}CuN_6O_8$
M_r	1016.504	982.448	977.450	943.395	936.615
Crystal system	Monoclinic	Triclinic	Monoclinic	Triclinic	Monoclinic
Space group	$P2_1/c$	$P-1$	$P2_1/n$	$P-1$	$P2_1/n$
T/K	100(1)	100(1)	100(1)	100(1)	100(1)
$a/Å$	7.2566(2)	7.9291(3)	7.9338(1)	7.7476(4)	7.8787(1)
$b/Å$	37.7315(9)	12.155(5)	10.2793(2)	11.6292(6)	10.3607(3)
$c/Å$	8.4952(3)	12.7150(5)	28.5066(5)	12.4652(7)	28.6114(5)
$\alpha/°$	90	76.947(3)	90	82.283(4)	90
$\beta/°$	103.354(4)	72.828(3)	94.659(1)	74.404(4)	94.888(1)
$\gamma/°$	90	70.520(3)	90	76.633(4)	90
$V/Å^3$	2263.11(12)	1092.7(5)	2317.14(7)	1049.32(10)	2327.02(8)
Z	2	1	2	1	2
$\lambda/Å$	1.54186	1.54186	1.54186	1.54186	1.54186
Abs. correction	Multi-scan, LANA	Multi-scan, LANA	Multi-scan, LANA	Multi-scan, LANA	Multi-scan, LANA
μ/mm^{-1}	1.438	1.448	2.224	2.414	1.158
Crystal size/mm	$0.35 \times 0.15 \times 0.12$	$0.36 \times 0.09 \times 0.09$	$0.35 \times 0.32 \times 0.25$	$0.25 \times 0.21 \times 0.05$	$0.32 \times 0.25 \times 0.18$
$\rho_{calc}/g.cm^{-3}$	1.492	1.492	1.401	1.493	1.337
S	1.015	1.096	1.064	1.047	1.073
R_1 [$I > 2\sigma(I)$]	0.0283	0.0178	0.0191	0.0237	0.0240
wR_2 [all data]	0.0739	0.0372	0.0486	0.0581	0.0556
$\Delta\rangle_{max}, \Delta\rangle_{min}/e$ Å^{-3}	0.74, −0.30	0.40, −0.19	0.18, −0.38	0.25, −0.38	0.34, −0.30
CCDC	2202673	2202674	2202675	2202676	2202677

The trifluoromethyl group of the niflumate ligand in the crystal structure of **2** was disordered in three parts (Supplementary Figure S4), represented by atoms with occupation factors of 0.51(2) (green lines), 0.29(2) (orange lines) and 0.20(2) (violet lines). The occupation factors were specified using the SUMP instruction. HAR refinement was carried out using restraints C–F and F···F distances using SADI instructions. All fluorine atoms were refined anisotropically with RIGU instruction restraints. Isostructural complexes **3** and **5** contained similarly disordered tolfenamate (**3**) (Supplementary Figure S5) or mefenamate (**5**) (Supplementary Figure S7) ligands in two positions (green lines for main parts, and violet lines for minor parts) with a ratio of occupancy factors of 0.850(1)/0.150(1) for **3** and 0.710(1)/0.290(1) for **5**. The disordered parts of the tolfenamate or mefenamate ligands of both compounds were modeled and refined with constraints and restraints using the SAME instructions, supplemented with SADI/DFIX instructions for C–H distances and RIGU and EADP instructions for non-hydrogen atoms.

3.4. Hirshfeld Surface Analysis

Crystal Explorer [64] was used to calculate the Hirshfeld surfaces [65] and associated fingerprint plots [39,66]. The Hirshfeld surface for complex **2** was calculated including all three orientations of the disordered –CF₃ group with their partial occupancies. The Hirshfeld surfaces of strongly disordered complexes **3** and **5** were calculated separately for the main and minor disordered components.

3.5. Electrochemical Study

The redox behavior of the studied complexes (10^{-4} M for all substances) was determined via a cyclic voltammetry study using an argentochloride reference electrode, platinum counter electrode and boron-doped diamond (BDD) working electrode (diameter of 3 mm, boron doping level of 1000 ppm, Windsor Scientific Ltd., UK). All voltammetric curves were registered at the potential range from –1.0 to +1.5 V using a scan rate of 100 mV/s.

3.6. Interactions with ct-DNA

3.6.1. Absorption Titrations

Interactions of the prepared complexes **1–4** with DNA were studied with UV-Vis monitored absorption titrations. In this experiment, a DNA stock solution was prepared by dissolving 6 mg of DNA in 5 mL of citrate buffer (containing 15 mM of sodium citrate and 150 mM of NaCl at pH = 7.0). The concentration of DNA was then determined with UV-Vis spectroscopy, where 0.150 mL of stock solution of DNA was added to 2.85 mL of citrate buffer, using a molar absorption coefficient of DNA at 260 nm (6 600 $M^{-1}cm^{-1}$) [67]. The ratio of absorbance at 260 nm and at 280 nm indicated that the DNA was sufficiently pure from proteins [68]. Increasing concentrations of DNA were then added to a buffer/DMSO solution (<1% DMSO) of the corresponding complex. The magnitudes of the binding strength of the complex–DNA interactions expressed as the intrinsic binding constant K_b were calculated with the ratio of slope to the intercept in the plots [DNA]/(ε_A-ε_f) versus [DNA], according to the Wolfe–Shimmer equation (Equation (1)):

$$\frac{[DNA]}{\left(\varepsilon_a - \varepsilon_f\right)} = \frac{[DNA]}{\left(\varepsilon_b - \varepsilon_f\right)} + \frac{1}{K_b\left(\varepsilon_b - \varepsilon_f\right)} \tag{1}$$

where the meaning of all symbols can be found elsewhere [48]. Control measurements with DMSO were performed, and no changes in the spectra of DNA were observed.

3.6.2. Fluorescence Quenching of EB-DNA Adduct

The ability of the prepared complexes to displace the standard intercalator ethidium bromide (EB) from the EB-DNA adduct was investigated with fluorescence spectroscopy. The EB-DNA adduct was prepared by adding 20 μM EB and 54 μM DNA in a buffer (15 mM of sodium citrate and 150 mM of NaCl at pH = 7.0). The possible intercalating effect of the compounds was studied by adding increasing concentrations of a corresponding complex into a solution of the DNA-EB complex. The fluorescence emission spectra were recorded in the range of 550–800 nm with an excitation wavelength of 515 nm. A decrease in the intensity of the EB-DNA emission band at 615 nm was monitored for complexes **1–4** and were correlated with the same measurement with DMSO. The quenching of the EB-DNA emission band by compounds **1–4** and DMSO was calculated via the Stern–Volmer equation (Equation (2))

$$I_0/I = 1 + k_q \tau_0 [Q] = 1 + K_{SV} [Q] \tag{2}$$

where k_q (M^{-1} s^{-1}) is the quenching constant of complexes **1–4**, K_{SV} (M^{-1}) is the value of the dynamic quenching constant, τ_0 is the average lifetime of the EB-DNA adduct in the absence of the quencher (23×10^{-9} s), and [Q] is the concentration of the quencher. I_0 is

the initial fluorescence intensity of the EB-DNA adduct, and I is the fluorescence intensity of the EB-DNA adduct after the addition of the complexes. K_{SV} can be obtained from the slope of the I_0/I versus $[Q]$ plot [21].

3.6.3. Viscosimetric Studies

Changes in the viscosity of the DNA solution (0.1 mM) were measured in the presence of increasing concentrations of the compounds in a buffer solution (15 mM of sodium citrate and 150 mM of NaCl at pH = 7.0) at a constant temperature 25 °C. The measurements were carried out using an ALPHA L Fungilab rotational viscometer equipped with an 18 mL ELVAS spindle, and the measurements were performed at 60 rpm. The relation between the relative solution viscosity (η/η_0) and DNA length (I/I_0) is given by Equation (3), where η and η_0 are the viscosities of DNA in the presence and absence of the studied complex.

$$\left(\frac{\eta}{\eta_0}\right)^{1/3} = \frac{I}{I_0} \tag{3}$$

3.7. SOD Mimetic Activity

The ability of the copper complexes to scavenge superoxide radical anions was determined using the NBT (Nitro-Blue Tetrazolium) indirect colorimetric test, in which the xanthine/xanthine oxidase (X/XO) system was used as a superoxide-generating system [27]. The extent of NBT reduction was monitored spectrophotometrically by measuring the absorbance at 560 nm for 5 min. The reaction mixture contained 0.2 mM of xanthine and 0.6 mM of NBT in 0.1 mM of a sodium phosphate buffer at a pH of 7.8 and at 25 °C with a volume of 3 mL. The tested compounds were dissolved in DMSO. The concentration of xanthine-oxidase (XO) was experimentally designed to give an absorbance change ($\Delta A/min$) between 0.035 and 0.045. Inhibitory concentrations were calculated from the slopes of individual curves with Equation (4):

$$IC = \frac{b_0 - b}{b_0} \tag{4}$$

where b_0 is the slope of the non-inhibited system, and b is the slope of the inhibited system with a corresponding complex concentration. IC_{50} values were obtained from the graphical dependence of the inhibitory concentration and the concentration of the complex [42]. An investigation of the formation of Cu(I) ions after reduction with the superoxide radical anion was conducted via UV-Vis spectroscopy using a specific Cu(I) chelating agent, neocuproine (2,9-dimethyl-1,10-phenanthroline). Potassium superoxide (KO_2) was used as a source of the superoxide anion together with 18-crown-6-ether, which acted as a stabilizing agent. The absorption spectra were measured in the range of 400–800 nm after the addition of 500 µL of 1 mM of neocuproine and 500 µL of 1 mM of potassium superoxide DMSO solution to 500 µL of 1 mM of complex **1–4** DMSO solution using the Specord 250 plus UV/Vis spectrometer [27].

3.8. Bovine Serum Albumin (BSA) Binding Studies

The albumin binding studies for complexes **1–4** were performed with tryptophan fluorescence emission quenching experiments using BSA (30 µM) in a buffer solution (containing 15 mM of trisodium citrate and 150 mM of NaCl at a pH of 7.0). The quenching of the emission intensity of the tryptophan residues of BSA at 336 nm was monitored using increasing concentrations of complexes **1–4** as quenchers [21]. The fluorescence emission spectra were recorded in the range of 300–420 nm with an excitation wavelength of 280 nm. The values of the Stern–Volmer constant K_{SV} (in M^{-1}), the BSA quenching constant k_q (in $M^{-1} s^{-1}$) and the BSA binding constant K_{BSA} (in M^{-1}) for the interaction of

the compounds with BSA were derived with the Stern–Volmer (Equation (2)) and Scatchard equations (Equation (5)).

$$\frac{\Delta I / I_0}{[Q]} = nK - K\frac{\Delta I}{I_0} \tag{5}$$

where K (in M^{-1}) is the value of the bovine serum albumin constant K_{BSA}, n is the number of binding sites per albumin, and $[Q]$ is the concentration of the quencher. I_0 is the initial fluorescence intensity of the tryptophan residues of albumin, and I is the fluorescence intensity of albumin after the addition of the complexes. K_{BSA} can be obtained from the slope of the $\Delta I/I_0/[Q]$ versus $\Delta I/I_0$, and n can be calculated from the intercept [29].

3.9. Anticancer Studies

3.9.1. Cell Culture

Human lung cancer cells (A549), human breast cancer cells (MCF-7) and human glioblastoma cells (U-118MG) were purchased from the American Type Culture Collection (Manassas, VA, USA) and were maintained in Dulbecco's Modified Eagle Medium (DMEM, Life Technologies, Inc., Rockville, MD, USA) containing 10% fetal bovine serum, 100 μg/mL of streptomycin and 100 U/mL of penicillin G at 37 °C in a humidified atmosphere of 5% CO_2/95% air. Human lung fibroblasts (MRC-5) (ECACC, Salisbury, UK) were cultured in MEM containing 10% fetal bovine serum, 1% non-essential amino acids and 1% L-glutamine and penicillin–streptomycin mixture at 37 °C in a humidified atmosphere of 5% CO_2/95% air. For our experiments, cells were seeded on culture dishes or plates in the amounts described below. Cells at passage numbers 10–13 were used.

3.9.2. Cytotoxic Analysis

We determined the cytotoxic effects of four copper complexes **1**–**4** on carcinoma cells and healthy cells by using the MTT [3-(4,5-dimethylthiazol-2-yl)-2,5-diphenyltetrazolium bromide] colorimetric technique [69]. Cells were seeded (8×10^3 cells/200 μL well) in individual wells of 96-multiwell plates. We added different concentrations of copper complexes (20–1000 μmol/L) to the cells and incubated them for 24, 48 and 72 h at 37 °C (humidified atmosphere of 5% CO_2/95% air). After 72 h, the cells were treated with the MTT solution (5 mg/mL) in PBS (phosphate-buffered saline) (20 μL) for 4 h. The dark crystals of formazan, formed in intact cells, were dissolved in DMSO (dimethyl sulfoxide) (200 μL). The plates were shaken for 15 min, and the optical density was determined at 490 nm using a MicroPlate Reader (Biotek, Winooski, VT, USA). All dye exclusion tests were performed three times.

3.9.3. Genotoxic Analysis

We determined DNA strand breaks in MCF-7 cells after 72 h of incubation with complex **4** at an IC_{50} value. DNA strand breaks were measured using the alkaline comet assay [70]. Cells were resuspended in 400 μL of 0.8% low-melting-point agarose in PBS at 37 °C and pipetted onto a frosted microscope slide precoated with 100 μL of 1% normal-melting-point agarose. Slides with layers of cells in agarose were incubated in a refrigerator for 10 min (4 °C) and then immersed in a lysis solution (2.5 mol/L NaCl, 100 mmol/L, Na_2EDTA, 10 mmol/l Tris, 1% Triton, pH of 10) for 1 h to remove cell membranes. After lysis, slides were placed in a horizontal electrophoresis tank containing an electrophoresis solution (1 mmol/L Na_2EDTA, 300 mmol/L NaOH, pH of 13) at 4 °C for 40 min (DNA uncoiling). Electrophoresis measurements were performed in the same solution at 25 V, 300 mA and 4 °C for 30 min. The slides were washed three times for 5 min at 4 °C with a neutralizing buffer (0.4 mmol/L Tris, pH of 7.5) before staining with 20 μL of 4′,6-diamidine-2-phenylindole dihydrochloride (DAPI, 1 μg/mL solution in distilled water). Comets were viewed with fluorescence microscopy after staining with DAPI.

3.9.4. Statistical Analysis

The results obtained from the comet assay are shown as the arithmetic means $\pm$ the standard deviation (SD). The significance of differences between values acquired with the comet assay was evaluated with Student's *t*-test to determine if the values were statistically different from those of the control: * $p < 0.05$.

4. Conclusions

In this report, we discuss the synthesis, structural and spectroscopic characterization and biological activity of five copper (II) complexes with *N, N*-dietlylnicotinamide and fenamate ligands. The following complexes were prepared: $[Cu(fluf)_2(dena)_2(H_2O)_2]$ (**1**), $[Cu(nifl)_2(dena)_2]$ (**2**), $[Cu(tolf)_2(dena)_2(H_2O)_2]$ (**3**), $[Cu(clon)_2(dena)_2]$ (**4**) and $[Cu(mef)_2(dena)_2(H_2O)_2]$ (**5**). The complexes were characterized in terms of their elemental composition, structure, physico-chemical and biological properties. The crystal structures of the studied compounds were refined using a more accurate aspherical HAR method using data measured with a high redundancy at 100 K. The crystal structures revealed the different influences of benzene versus the pyridine ring on the possibility of the coplanarity of fenamate anions and thus also the possibility of forming hydrogen bonds and/or π–π stacking interactions. The studied complexes are monomeric, forming a distorted tetragonal bipyramidal stereochemistry around a central copper ion. Complex **1** and the isostructural complexes **3** and **5** crystallize in a monoclinic system with a $P2_1/c$ (**1**) or $P2_1/n$ (**3,5**) space group, while the nearly isostructural complexes **2** and **4** crystallize in a triclinic system with a *P*-1 space group. The fenamate ligands are coordinated to a copper atom either monodentately (**1**, **3**, **5**) or asymmetrical chelating bidentately (**2**, **4**). The complex molecules of **1–5** are connected in *1D* supramolecular chains by means of intermolecular hydrogen bonds and π–π stacking interactions. In addition, Hirshfeld surface analysis was used to quantitatively identify the intermolecular interactions in the crystal structures of all five compounds.

The EPR spectra of solid-state and frozen DMSO solutions of **1–5** were monomeric with axial symmetry and with a relative ordering of axial *g* factors of $g_{\parallel} > g_{\perp} \sim g_e$, showing either resolved or unresolved copper parallel hyperfine interactions. The similarity between the solid and solution EPR data suggests a resemblance in the geometries of the studied complexes in accordance with the observed crystal structures.

The SOD mimetic activity of the complexes was studied indirectly using an NBT assay, and the complexes were characterized by means of IC_{50} (1.41–3.46 µM). The obtained inhibition concentrations showed that the complexes are good SOD mimetics, with the best results obtained for **2** and **4**. The cyclic voltammetry results confirmed the quasi-reversible nature of the redox processes on the studied complexes, with values of $E_{1/2}$ that are in agreement with the SOD mimetic activity of the complexes. The interactions of complexes **1–4** with neocuproine and KO_2 were, again, in agreement with the SOD data and support the hypothesis of the redox cycling mechanism between the studied copper complexes and superoxide.

The potential of complexes **1–4** to interact with DNA was also investigated. Absorption titration studies pointed to the intercalative binding of our complexes to DNA with a relatively strong binding constant of K_b (10^5), especially in cases of **4** and **1**. In the viscosity measurements, we observed a continual increase in the relative DNA viscosity for all four complexes, indicating a possible intercalation mechanism of interaction between the complexes and DNA. The intercalating ability of the complexes toward DNA was also studied with an ethidium-bromide-displacement-fluorescence-based method. The results revealed moderate intercalative ability toward DNA. In addition, the affinity of the complexes to interact with bovine serum albumin was studied, showing tight and reversible mutual interactions, as revealed by relatively high binding constants K_{BSA} (of order 10^5) and quenching constants k_q (of order 10^{13}) for all four complexes. In the case of comparing the structures and biological activity of structurally similar complexes **2**, **4** vs. **1**, **3**, no distinct trend was observed.

The cytotoxic activity of the studied complexes revealed that only complex **4** exhibited cytotoxic activity on the MCF-7 tumor cell line after 72 h of exposure with an IC_{50} value of 0.57×10^{-4} M.

Supplementary Materials: The following supporting information can be downloaded at https://www.mdpi.com/article/10.3390/inorganics11030108/s1: Figures S1–S20: IR spectra; UV-Vis spectra; crystal structures, 3D Hirshfeld surfaces, 2D fingerprints plots; Scatchard plots; Table S1: Hydrogen bond parameters. checkCIF and crystallographic data (excluding structure factors) for the structures reported in this paper were deposited into the Cambridge Crystallographic Data Centre as supplementary publications, nos. CCDC-2202673–2202677. Copies of the data can be obtained free of charge on application to the CCDC, 12 Union Road, Cambridge CB2 1EZ, UK [fax: (internat.) +44 1223/336033; e-mail: deposit@ccdc.cam.ac.uk].

Author Contributions: Conceptualization, J.Š. and M.P.; methodology, M.P., J.V. and J.Š.; investigation, M.P., M.S., K.K., Ľ.Š., J.M., M.V. and J.Š.; writing—original draft preparation, J.Š.; writing—review and editing, J.V., J.M. and M.V.; visualization, J.Š. and M.P.; supervision, J.Š. All authors have read and agreed to the published version of the manuscript.

Funding: Slovak grant agencies (VEGA 1/0482/20, VEGA 1/0159/20, VEGA 1/0686/23, APVV-19-0087, APVV-18-0016 and VEGA 1/0145/20) are acknowledged for their financial support.

Conflicts of Interest: The authors declare no conflict of interest. The funders had no role in the design of the study; in the collection, analyses, or interpretation of data; in the writing of the manuscript; or in the decision to publish the results.

References

1. Bindu, S.; Mazumder, S.; Bandyopadhyay, U. Non-steroidal anti-inflammatory drugs (NSAIDs) and organ damage: A current perspective. *Biochem. Pharmacol.* **2020**, *180*, 114147. [CrossRef] [PubMed]
2. Ramos-Inza, S.; Carolina, R.A.; Sanmartin, C.; Sharma, A.K.; Plano, D. NSAIDs: Old Acquaintance in the Pipeline for Cancer Treatment and Prevention-Structural Modulation, Mechanisms of Action, and Bright Future. *J. Med. Chem.* **2021**, *64*, 16380–16421. [CrossRef]
3. Weder, J.E.; Dillon, C.T.; Hambley, T.W.; Kennedy, B.J.; Lay, P.A.; Biffin, J.R.; Regtop, H.L.; Davies, N.M. Copper complexes of non-steroidal anti-inflammatory drugs: An opportunity yet to be realized. *Coord. Chem. Rev.* **2002**, *232*, 95–126. [CrossRef]
4. Matsui, H.; Shimokawa, O.; Kaneko, T.; Nagano, Y.; Rai, K.; Hyodo, L. The pathophysiology of non-steroidal anti-inflammatory drug (NSAID)-induced mucosal injuries in stomach and small intestine. *J. Clin. Biochem. Nutr.* **2011**, *48*, 107–111. [CrossRef] [PubMed]
5. Psomas, G. Copper(II) and zinc(II) coordination compounds of non-steroidal anti-inflammatory drugs: Structural features and antioxidant activity. *Coord. Chem. Rev.* **2020**, *412*, 213259. [CrossRef]
6. Sun, J.-F.; Xu, Y.-J.; Kong, X.-H.; Su, Y.; Wang, Z.-Y. Fenamates inhibit human sodium channel Nav1.7 and Nav1.8. *Neurosci. Lett.* **2019**, *696*, 67–73. [CrossRef] [PubMed]
7. Hill, J.; Zawia, N.H. Fenamates as Potential Therapeutics for Neurodegenerative Disorders. *Cells* **2021**, *10*, 702. [CrossRef] [PubMed]
8. Prasher, P.; Sharma, M. Medicinal chemistry of anthranilic acid derivatives: A mini review. *Drug Dev. Res.* **2021**, *82*, 945–958. [CrossRef]
9. Moncol, J.; Múdra, M.; Lönnecke, P.; Hewitt, M.; Valko, M.; Morris, H.; Švorec, J.; Melnik, M.; Mazúr, M.; Koman, M. Crystal structures and spectroscopic behavior of monomeric, dimeric and polymeric copper(II) chloroacetate adducts with isonicotinamide, *N*-methylnicotinamide and *N,N*-diethylnicotinamide. *Inorg. Chim. Acta* **2007**, *360*, 3213–3225. [CrossRef]
10. Choi, H.-E.; Choi, J.-H.; Lee, J.Y.; Kim, J.H.; Kim, J.H.; Lee, J.K.; Kim, G.I.; Park, Y.; Chi, Y.H.; Paik, S.H.; et al. Synthesis and evaluation of nicotinamide derivative as anti-angiogenic agents. *Bioorganic Med. Chem. Lett.* **2013**, *23*, 2083–2088. [CrossRef]
11. Peng, M.; Shi, L.; Ke, S. Nicotinamide-based diamides derivatives as potential cytotoxic agents: Synthesis and biological evaluation. *Chem. Cent. J.* **2017**, *11*, 109. [CrossRef]
12. Banti, C.N.; Hadjikakou, S.K. Non-steroidal anti-inflammatory drugs (NSAIDs) in metal complexes and their effect at the cellular level. *Eur. J. Inorg. Chem.* **2016**, *2016*, 3048–3071. [CrossRef]
13. Khan, H.Y.; Parveen, S.; Yousuf, I.; Tabassum, S.; Arjmand, F. Metal complexes of NSAIDs as potent anti-tumor chemotherapeutics: Mechanistic insights into cytotoxic activity via multiple pathways primarily by inhibition of COX-1 and COX-2 enzymes. *Coord. Chem. Rev.* **2022**, *453*, 214316. [CrossRef]
14. Boodram, J.N.; Mcgregor, I.J.; Bruno, P.M.; Cressey, P.B.; Hemann, M.T.; Suntharalingam, K. Breast Cancer Stem Cell Potent Copper(II)-Non-Steroidal Anti-Inflammatory Drug Complexes. *Angew. Chem. Int. Ed.* **2016**, *55*, 2845–2850. [CrossRef]

15. Eskandari, A.; Boodram, J.N.; Cressey, P.B.; Lu, C.; Bruno, P.M.; Hemann, M.T.; Suntharalingam, K. The breast cancer stem cell potency of copper(II) complexes bearing nonsteroidal anti-inflammatory drugs and their encapsulation using polymeric nanoparticles. *Dalton Trans.* **2016**, *45*, 17867–17873. [CrossRef] [PubMed]

16. Johnson, A.; Iffland-Muhlhaus, L.; Northcote-Smith, J.; Singh, K.; Ortu, F.; Apfel, U.P.; Suntharalingam, K. A bioinspired redox-modulating copper(II)-macrocyclic complex bearing non-steroidal anti-inflammatory drugs with anti-cancer stem cell activity. *Dalton Trans.* **2022**, *51*, 5904–5912. [CrossRef] [PubMed]

17. Zehra, S.; Tabassum, S.; Arjmand, F. Biochemical pathways of copper complexes: Progress over the past 5 years. *Drug Discov. Today* **2021**, *26*, 1086–1096. [CrossRef]

18. Kumar, S.; Sharma, R.P.; Venugopalan, P.; Ferretti, V.; Tarpin, M.; Sayen, S.; Guillon, E. New copper(II) niflumate complexes with N-donor ligands: Synthesis, characterization and evaluation of anticancer potentional against human cell lines. *Inorg. Chim. Acta* **2019**, *488*, 260–268. [CrossRef]

19. Khan, H.Y.; Zehra, S.; Parveen, S.; Yousuf, I.; Tabassum, S.; Arjmand, F. New ionic Cu(II) and Co(II) DACH-flufenamate conjugate complexes: Spectroscopic characterization, single X-ray studies and cytotoxic activity on human cancer cell lines. *ChemistrySelect* **2018**, *3*, 12764–12772. [CrossRef]

20. Nnabuike, G.G.; Salunke-Gawali, S.; Patil, A.S.; Butcher, R.J.; Obaleye, J.A.; Ashtekar, H.; Prakash, B. Copper(II) complexes containing derivative of aminobenzoic acid and nitrogen-rich ligans: Synthesis, characterization and cytotoxic potential. *J. Mol. Struct.* **2023**, *1279*, 135002. [CrossRef]

21. Malis, G.; Geromichalou, E.; Geromichalos, G.D.; Hatzidimitriou, A.G.; Psomas, G. Copper(II) complexes with non-steroidal anti-inflammatory drugs: Structural characterization, in vitro and in silico biological profile. *J. Inorg. Biochem.* **2021**, *224*, 111563. [CrossRef] [PubMed]

22. Sharma, R.P.; Kumar, S.; Venugopalan, P.; Ferretti, V.; Tarushi, A.; Psomas, G.; Witwicki, M. New copper(II) complexes of anti-inflammatory drug mefenamic acid: A concerted study including synthesis, physicochemical characterization and their biological evaluation. *RSC Adv.* **2016**, *6*, 88546–88558. [CrossRef]

23. Tolia, C.; Papadopoulos, A.N.; Raptopoulou, C.P.; Psycharis, V.; Garino, C.; Salassa, L.; Psomas, G. Copper(II) interacting with non-steroidal antiinflammatory drug flufenamic acid: Structure, antioxidant activity and binding to DNA and albumins. *J. Inorg. Biochem.* **2013**, *123*, 53–65. [CrossRef]

24. Dimiza, F.; Fountoulaki, S.; Papadopoulos, A.N.; Kontogiorgis, C.A.; Tangoulis, V.; Raptopoulou, C.P.; Psycharis, V.; Terzis, A.; Kessissoglou, D.P.; Psomas, G. Non-steroidal antiinflammatory drug-copper(II) complexes: Structure and biological perpectives. *Dalton Trans.* **2011**, *40*, 8555–8568. [CrossRef]

25. Barmpa, A.; Perontsis, S.; Hatzidimitriou, A.G.; Psomas, G. Copper(II) complexes with meclofenamate ligands: Structure, interaction with DNA and albumins, antioxidant and anticholinergic activity. *J. Inorg. Biochem.* **2011**, *217*, 111357. [CrossRef]

26. Tarushi, A.; Perontsis, S.; Hatzidimitriou, A.G.; Papadopoulos, A.N.; Kessissoglou, D.P.; Psomas, G. Copper(II) complexes with the non-steroidal anti-inflammatory drug tolfenamic acid: Structure and biological features. *J. Inorg. Biochem.* **2015**, *149*, 68–79. [CrossRef] [PubMed]

27. Simunkova, M.; Lauro, P.; Jomova, K.; Hudecova, L.; Danko, M.; Alwasel, S.; Alhazza, I.M.; Rajcaniova, S.; Kozovska, Z.; Kucerova, L.; et al. Redox-cycling and intercalating properties of novel mixed copper(II) complexes with non-steroidal anti-inflammatory drugs tolfenamic, mefenamic and flufenamic acids and phenanthroline functionality: Structure, SOD-mimetic activity, interaction with albumin, DNA damage study and anticancer activity. *J. Inorg. Biochem.* **2019**, *194*, 97–113. [CrossRef]

28. Jozefíková, F.; Perontsis, S.; Koňáriková, K.; Švorc, Ľ.; Mazúr, M.; Psomas, G.; Moncol, J. In vitro biological activity of copper(II) complexes with NSAIDs and nicotinamide: Characterization, DNA- and BSA-interaction study and anticancer activity. *J. Inorg. Biochem.* **2022**, *228*, 111696. [CrossRef]

29. Jozefíková, F.; Perontsis, S.; Šimunková, M.; Barbieriková, Z.; Švorc, Ľ.; Valko, M.; Psomas, G.; Moncol, J. Novel copper(II) complexes with fenamates and isonicotinamide: Structure and properties, and interactions with DNA and serum albumin. *New J. Chem.* **2020**, *44*, 12827–12842. [CrossRef]

30. Melník, M.; Potočňak, I.; Macášková, Ľ.; Mikloš, D.; Holloway, C.E. Spectral study of copper(II) flufenamates: Crystal and molecular structure of bis(flufenamato)di(*N,N*-diethylnicotinamide)di(aqua)copper(II). *Polyhedron* **1996**, *15*, 2159–2164. [CrossRef]

31. Švorec, J.; Lörinc, Š.; Moncol, J.; Melník, M.; Koman, M. Structural and spectroscopic characterization of copper(II) tolfenamate complexes. *Transit. Met. Chem.* **2009**, *34*, 703–710. [CrossRef]

32. Melník, M.; Koman, M.; Macášková, Ľ.; Glowiak, T. Spectral and magnetic properties of copper(II) mefenamates: Crystal and molecular structure of bis(mefenamato)di(N,N-diethylnicotinamide)di(aqua)copper(II). *J. Coord. Chem.* **1998**, *44*, 163–172. [CrossRef]

33. Koman, M.; Melník, M.; Glowiak, T. Structure, spectral and magnetic behaviours of copper(niflumato)$_2$(N,N-diethylnicotinamide)$_2$. *J. Coord. Chem.* **1998**, *44*, 133–139. [CrossRef]

34. Nakamoto, K. *Infrared and Raman Spectra of Inorganic and Coordination Compounds, Part B*, 6th ed.; John Wiley and Sons, Inc.: Hoboken, NJ, USA, 2009; pp. 1–199.

35. Hathaway, B.J.; Billing, D.E. The electronic properties and stereochemistry of mono-nuclear complexes of the copper(II) ion. *Coord. Chem. Rev.* **1970**, *5*, 143. [CrossRef]

36. Moncol, J.; Mudra, M.; Lönnecke, P.; Koman, M.; Melník, M. Copper(II) halogenopropionates: Low-temperature crystal and molecular structure of bis(2,2-dichloropropionato)-di(methyl-3-pyridylcarbamate)copper(II) and bis(2-bromopropionato)-di(2-pyridylmethanol)copper(II). *J. Coord. Chem.* **2004**, *57*, 1065–1078. [CrossRef]

37. Korabik, M.; Repická, Z.; Martiška, L.; Moncol, J.; Švorec, J.; Padelkova, Z.; Lis, T.; Mazur, M.; Valigura, D. Hydrogen-Bond-Based Magnetic Exchange Between mu-Diethylnicotinamide(aqua)bis(X-salicylato)copper(II) Polymeric Chains. *Z. Anorg. Allg. Chem.* **2011**, *637*, 224–231. [CrossRef]

38. Spackman, M.A.; Jayalitaka, D. Hirshfeld surface analysis. *CrystEngComm* **2009**, *11*, 19–32. [CrossRef]

39. Spackman, M.A.; McKinnon, J.J. Fingerprinting intermolecular interactions in molecular crystals. *CrystEngComm* **2002**, *4*, 378–392. [CrossRef]

40. Sakaguchi, U.; Addison, A.W. Spectroscopic and redocx studies of some copper (II) ccomplexes with biomimetic donor atoms–Implication for protein copper centers. *J. Chem. Soc. Dalton Trans.* **1979**, 600–608. [CrossRef]

41. Puchonova, M.; Švorec, J.; Švorc, L.; Pavlik, J.; Mazur, M.; Dlhan, L.; Ruzickova, Z.; Moncol', J.; Valigura, D. Synthesis, spectral, magnetic properties, electrochemical evaluation and SOD mimetic activity of four mixed-ligand Cu(II) complexes. *Inorg. Chim. Acta* **2017**, *455*, 298–306. [CrossRef]

42. Kovala-Demertzi, D.; Galani, A.; Demertzis, M.A.; Skoulika, S.; Kotoglou, C. Binuclear copper(II) complexes of tolfenamic: Synthesis, crystal structure, spectroscopy and superoxide dismutase activity. *J. Inorg. Biochem.* **2004**, *98*, 358–364. [CrossRef] [PubMed]

43. Sheng, Y.; Abreu, I.A.; Cabelli, D.E.; Maroney, M.J.; Miller, A.; Teixeira, M.; Valentine, J.S. Superoxide Dismutases and Superoxide Reductases. *Chem. Rev.* **2014**, *114*, 3854–3918. [CrossRef] [PubMed]

44. Brezova, V.; Valko, M.; Breza, M.; Morris, H.; Telser, J.; Dvoranova, D.; Kaiserova, K.; Varecka, L.; Mazur, M.; Leibfritz, D. Role of radicals and singlet oxygen in photoactivated DNA cleavage by the anticancer drug camptothecin: An electron paramagnetic resonance study. *J. Phys. Chem. B* **2003**, *107*, 2415–2425. [CrossRef]

45. Santini, C.; Pellei, M.; Gandin, V.; Porchia, M.; Tisato, F.; Marzano, C. Advances in Copper Complexes as Anticancer Agents. *Chem. Rev.* **2014**, *114*, 815–862. [CrossRef]

46. Erxleben, A. Interactions of copper complexes with nucleic acids. *Coord. Chem. Rev.* **2018**, *360*, 92–121. [CrossRef]

47. Andrezalova, L.; Orszaghova, Z. Covalent and noncovalent interactions of coordination compounds with DNA: An overview. *J. Inorg. Biochem.* **2021**, *225*, 111624. [CrossRef]

48. Sirajuddin, M.; Ali, S.; Badshah, A. Drug-DNA interactions and their study by UV-Visible, fluorescence spectroscopies and cyclic voltametry. *J. Photochem. Photobiol. B Biol.* **2013**, *124*, 1–19. [CrossRef]

49. Smolkova, R.; Smolko, L.; Samol'ova, E.; Dusek, M. Co(II) fenamato, tolfenamato and niflumato complexes with neocuproine: Synthesis, crystal structure, spectral characterization and biological activity. *J. Mol. Struct.* **2023**, *1272*, 134172. [CrossRef]

50. Arkel, Y.S.; Schrogie, J.J.; Williams, R. Effect of clonixin and aspirin on platelet-aggregation in human volunteers. *J. Clin. Pharmacol.* **1976**, *16*, 30–33. [CrossRef]

51. Spector, D.; Krasnovskaya, O.; Pavlov, K.; Erofeev, A.; Gorelkin, P.; Beloglazkina, E.; Majouga, A. Pt(IV) Prodrugs with NSAIDs as Axial Ligands. *Int. J. Mol. Sci.* **2021**, *22*, 3817. [CrossRef]

52. Ozarowski Andrzej, Spin Software (SpinP.exe). Available online: https://nationalmaglab.org/user-facilities/emr/software/ (accessed on 5 January 2016).

53. Kožišková, J.; Hahn, F.; Richter, J.; Kožíšek, J. Comparison of different absorption corrections on the model structure of tetrakis(μ_2-acetato)-diaqua-di-copper(II). *Acta Chim. Slovaca* **2016**, *9*, 136–146. [CrossRef]

54. Sheldrick, G.M. *SHELXT*—Integrated space-group and crystal-structure determination. *Acta Crystallogr. A* **2015**, *71*, 3–8. [CrossRef] [PubMed]

55. Palatinus, L.; Chapuis, G. *SUPERFLIP*—A computer program for the solution of crystal structures by charge flipping in arbitrary dimensions. *J. Appl. Crystallogr.* **2007**, *40*, 786–790. [CrossRef]

56. Burla, M.C.; Caliandro, R.; Carrozzini, B.; Cascarano, G.L.; Cuocci, C.; Giacovazzo, C.; Mallamo, M.; Mazzone, A.; Polidori, G.G. Crystal structure determination and refinement *via SIR2014*. *J. Appl. Crystallogr.* **2015**, *48*, 306–309. [CrossRef]

57. Sheldrick, G.M. Crystal structure refinement with *SHELXL*. *Acta Crystallogr. C* **2015**, *71*, 3–8. [CrossRef]

58. Neese, F. Software update the ORCA program system, version 4.0. *WIREs Comput. Mol. Sci.* **2018**, *8e*, 1327. [CrossRef]

59. Balabanov, N.B.; Peterson, K.A. Systematically convergent basis sets for transition metals. I. All-electron correlation consistent basis sets for the *3d* elements Sc-Zn. *J. Chem. Phys.* **2005**, *123*, 064107. [CrossRef]

60. Adamo, C.; Barone, V. Toward reliable density functional methods without adjustable parameters: PBE0 model. *J. Chem. Phys.* **1999**, *110*, 6158–6170. [CrossRef]

61. Bourhis, L.J.; Dolomanov, O.V.; Gildea, R.J.; Howard, J.A.K.; Puschmann, H. The anatomy of a comprehensive constrained, restrained refinement program for the modern computing environment—*Olex2* dissected. *Acta Crystallogr. A* **2015**, *71*, 59–75. [CrossRef]

62. Kleemiss, F.; Dolomanov, O.V.; Bodensteiner, M.; Peyerimhoff, N.; Midgley, L.; Bourhis, L.J.; Genoni, A.; Malaspina, L.A.; Jayatilaka, D.; Spencer, J.L.; et al. Accurate crystal structures and chemical properties from NoSpherA2. *Chem. Sci.* **2021**, *12*, 1675–1692. [CrossRef]

63. Dolomanov, O.V.; Bourhis, L.J.; Gildea, R.J.; Howard, J.A.K.; Puschmann, H. *OLEX2*: A complete structure solution, refinement and analysis program. *J. Appl. Crystallogr.* **2009**, *42*, 339–341. [CrossRef]

64. Spackman, P.R.; Turner, M.J.; McKinnon, J.J.; Wolff, S.K.; Grimwood, D.J.; Jayatilaka, D.; Spackman, M.A. *CrystalExplorer*: A program for Hirshfeld surface analysis, visualization and quantitative analysis of molecular crystals. *J. Appl. Crystallogr.* **2021**, *54*, 1006–1011. [CrossRef]
65. Hirshfeld, F.L. Bonded-atom fragments for describing molecular charge densities. *Theor. Chim. Acta* **1977**, *44*, 129–138. [CrossRef]
66. Parkin, A.; Barr, G.; Dong, W.; Gilmore, C.J.; Jayalitaka, D.; McKinnon, J.J.; Spackman, M.A.; Wilson, C.C. Comparing entire crystal structures: Structural genetic fingerprinting. *CrystEngComm* **2007**, *9*, 648–652. [CrossRef]
67. Wolfe, A.; Shimer, G.H., Jr.; Meehan, T. Polycyclic aromatic hydrocarbons physically intercalate into duplex regions of denatured DNA. *Biochemistry* **1987**, *26*, 6392–6396. [CrossRef] [PubMed]
68. Pyle, A.M.; Rehmann, J.P.; Meshoyrer, R.; Kumar, C.V.; Turro, N.J.; Barton, J.K. Mixed-ligand complexes of ruthenium(II)—Factors governing binding to DNA. *J. Am. Chem. Soc.* **1989**, *111*, 3051–3058. [CrossRef]
69. Carmichael, J.; Degraff, W.G.; Gazdar, A.F.; Minna, J.D.; Mitchell, J.B. Evaluation of a tetrazolium-based semiautomated coloimetric assay—Assesament of chemosensitivity testing. *Cancer Res.* **1987**, *47*, 936–942.
70. Collins, A.R.; Dobson, V.L.; Dusinska, M.; Kennedy, G.; Stetina, R. Comet assay: What can it really tell us? *Mutat. Res.* **1997**, *375*, 183–193. [CrossRef]